

8-19-2024

Macro–Micro-Coupled Simulations of Bead–Spring Breaking-Reforming Networks

Andrei Medved
University of South Carolina

Follow this and additional works at: <https://scholarcommons.sc.edu/etd>



Part of the [Applied Mathematics Commons](#)

Recommended Citation

Medved, A.(2024). *Macro–Micro-Coupled Simulations of Bead–Spring Breaking-Reforming Networks*. (Doctoral dissertation). Retrieved from <https://scholarcommons.sc.edu/etd/7801>

This Open Access Dissertation is brought to you by Scholar Commons. It has been accepted for inclusion in Theses and Dissertations by an authorized administrator of Scholar Commons. For more information, please contact digres@mailbox.sc.edu.

MACRO–MICRO–COUPLED SIMULATIONS OF BEAD–SPRING
BREAKING-REFORMING NETWORKS

by

Andrei Medved

Specialist

M. V. Lomonosov Moscow State University 2018

Submitted in Partial Fulfillment of the Requirements

for the Degree of Doctor of Philosophy in

Mathematics

College of Arts and Sciences

University of South Carolina

2024

Accepted by:

Dr. Paula Vasquez, Major Professor

Dr. Hong Wang, Committee Member

Dr. Changhui Tan, Committee Member

Dr. Dewei Wang, Committee Member

Dr. Ann Vail, Dean of the Graduate School

ABSTRACT

In this work we investigate the dynamic behavior of bead-spring polymer solutions in viscoelastic fluids, which are essential in industries like materials science, biotechnology, and pharmaceuticals. The study leverages GPU-accelerated simulations and detailed modeling of polymer chain dynamics at the mesoscale, which enables efficient analysis of intricate fluid behaviors and the microscale dynamics of polymer chains. Additionally, the research examines the breaking-reforming dynamics of polymer chains, crucial for understanding phenomena such as shear thinning and thickening. The findings have broad applications, from improving inkjet printing and 3D printing technologies to developing new drug delivery systems and biocompatible materials. This work aims to bridge the gap between microscale polymer dynamics and macroscale fluid behavior, contributing to the advancement of various technologies through a robust computational framework.

TABLE OF CONTENTS

| | |
|--|----|
| ABSTRACT | ii |
| LIST OF FIGURES | v |
| CHAPTER 1 INTRODUCTION | 1 |
| CHAPTER 2 COUPLING FLUID DYNAMICS USING LANGEVIN AND FOKKER- PLANCK EQUATIONS | 8 |
| 2.1 Langevin Approach | 10 |
| 2.2 Fokker–Planck Approach | 21 |
| CHAPTER 3 MICRO-MACRO DESCRIPTIONS OF VISCOELASTIC MATERIALS | 33 |
| 3.1 Conservation Equations | 33 |
| 3.2 Constitutive Modeling using Dumbbells Representations | 35 |
| 3.3 Numerical Schemes | 40 |
| 3.4 Macroscopic Closures of Dumbbell Models | 43 |
| 3.5 Results | 44 |
| CHAPTER 4 MODELING STIMULI RESPONSIVE MATERIALS | 49 |
| 4.1 Constitutive Modeling | 49 |
| 4.2 Numerical Schemes | 53 |
| 4.3 Results | 57 |

| | |
|----------------------------------|----|
| CHAPTER 5 DISCUSSION | 66 |
| 5.1 Concluding Remarks | 66 |
| 5.2 Future Work | 68 |
| BIBLIOGRAPHY | 69 |
| APPENDIX A | 74 |
| APPENDIX B | 76 |

LIST OF FIGURES

| | | |
|------------|---|----|
| Figure 1.1 | Coarse-grained representation of polymer molecules. Figure from [13] | 4 |
| Figure 2.1 | Relation between the Langevin equations (LE) and Fokker–Planck (FP) solutions. (A) LE solutions give particle positions as functions of time, each point represents a particle position at some time t . All particles have initial position $(0, 0)$ and follow different trajectories dictated by their respective noise history. (B) The distribution of particle positions can be summarized using a histogram. (C) FP solutions shows the probability of finding a particle at a given position as a function of time; darker color indicates a higher probability of finding a particle at that position. | 9 |
| Figure 2.2 | Evolution of 2D particle position for three different solutions of Equation (2.1). All three trajectories start from an initial position $(0, 0)$. In all three figures, $\Delta t = 0.001$ and the simulation ran for 1000 time steps. | 14 |
| Figure 2.3 | Mean squared displacement (MSD) in 1D, 2D, and 3D. Each line has been fitted to a function of the form $y = mx$, the best fitting value for the slope m is shown for each line. The slope for 1D is $2D = 0.019$, giving $D = 0.0095$, the slope for 2D gives $4D = 0.037 \Rightarrow D = 0.0093$, and for 3D it is $6D = 0.059 \Rightarrow D = 0.0098$. As a reference, the diffusion coefficient used to generate the particle trajectories is $D = 0.01$ | 18 |
| Figure 2.4 | Levels of description of a system, adapted from [43]. | 22 |
| Figure 2.5 | Probability density function (PDF) for position of particles diffusing via one-dimensional Brownian motion. Histograms correspond to LE data and solid lines corresponds to FP solutions. In this figure, $D = 10^{-2} \mu\text{m}^2/\text{s}$ | 27 |

| | | |
|------------|---|----|
| Figure 2.6 | PDF for position of particles diffusing via one-dimensional Brownian motion plus drift. Histograms correspond to generalized Langevin equations (GLE) data and solid lines corresponds to FP solutions. For comparison, FP solutions without drift are shown in dashed lines. In this figure, $D = 10^{-2} \mu\text{m}^2/\text{s}$, $u = 0.2 \mu/\text{s}$. | 29 |
| Figure 2.7 | LE and FP solutions for two-dimensional Brownian motion without external field. For both representations, $D = 10^{-2} \mu\text{m}^2/\text{s}$ and time is in seconds. For the LE representation, the total number of particles is 5×10^3 . | 30 |
| Figure 2.8 | LE and FP solutions for two-dimensional Brownian motion with constant drift. For both representations, $D = 10^{-2} \mu\text{m}^2/\text{s}$, $u = 0.2 \mu/\text{s}$ and time is in seconds. For the LE representation, the total number of particles is 5×10^3 . | 31 |
| Figure 2.9 | LE and FP solutions for two-dimensional Brownian motion with simple shear flow. For both representations, $D = 10^{-2} \mu\text{m}^2/\text{s}$, $U = 0.2 \mu/\text{s}$ and time is in seconds. For the LE representation, the total number of particles is 5×10^3 . | 32 |
| Figure 3.1 | Dumbbell chain configuration composed of $N - 1$ merged dumbbells. | 35 |
| Figure 3.2 | Single dumbbell configuration given by the coordinates of each dumbbell, \vec{r}_1 and \vec{r}_2 , or its center of mass, \vec{r}_c and end-to-end vector, \vec{Q} . | 36 |
| Figure 3.3 | Comparison of shear stress results for Hookean model and its UCM closure, $dt_{\text{macro}} = 10^{-1}$, $dt_{\text{micro}} = 10^{-5}$. | 45 |
| Figure 3.4 | Comparison of normal stress $N_1 = \tau_{xx} - \tau_{yy}$ results for Hookean model and its UCM closure, $dt_{\text{macro}} = 10^{-1}$, $dt_{\text{micro}} = 10^{-5}$. | 46 |
| Figure 3.5 | Comparison of shear stress results for FENE and FENE-P models, $dt_{\text{macro}} = 10^{-1}$, $dt_{\text{micro}} = 10^{-5}$, $b = 10^5$. | 47 |
| Figure 3.6 | Comparison of normal stress N_1 results for FENE and FENE-P models, $dt_{\text{macro}} = 10^{-1}$, $dt_{\text{micro}} = 10^{-5}$, $b = 10^5$. | 48 |
| Figure 4.1 | Double dumbbell configuration given by two free beads with a drag coefficient ζ and the junction with a drag coefficient 2ζ . | 50 |

| | | |
|------------|--|----|
| Figure 4.2 | Comparison of number of single dumbbells for Hookean models with reforming rate $\beta = 0.01$ and $\beta = 0.001$ | 58 |
| Figure 4.3 | Comparison of shear stress for Hookean models with reforming rate $\beta = 0.01$ and $\beta = 0.001$ | 59 |
| Figure 4.4 | Comparison of normal stress N_1 results for Hookean models with reforming rate $\beta = 0.01$ and $\beta = 0.001$ | 60 |
| Figure 4.5 | Comparison of normal stress N_2 results for Hookean models with reforming rate $\beta = 0.01$ and $\beta = 0.001$ | 61 |
| Figure 4.6 | Comparison of number of single dumbbells for FENE models with breaking rate $\tau_0 = 16$ and $\tau_0 = 1$ | 62 |
| Figure 4.7 | Comparison of shear stress for FENE models with breaking rate $\tau = 16$ and $\tau = 1$ | 63 |
| Figure 4.8 | Comparison of normal stress N_1 results for FENE models with breaking rate $\tau = 16$ and $\tau = 1$ | 64 |
| Figure 4.9 | Comparison of normal stress N_2 results for FENE models with breaking rate $\tau = 16$ and $\tau = 1$ | 65 |
| Figure B.1 | Histograms of particle positions for 1000 particles. (A) counts using 20 bins; (B) counts from (A) divided by total number of particles; (C) counts using 10 bins; (D) counts from (C) divided by total number of particles. | 76 |
| Figure B.2 | Normalized histogram of particle positions. The code used to generate these plots can be found in Appendix B. | 77 |
| Figure B.3 | Calculating probabilities using PDFs. | 78 |

CHAPTER 1

INTRODUCTION

Viscoelastic fluids, characterized by their intricate balance of viscous and elastic properties, are of particular interest due to their wide range of applications in industries such as materials science, biotechnology, and pharmaceuticals. Recent advancements in computational methods have opened new avenues for exploring these complex systems. The objective of this thesis is to explore the mathematical modeling of polymeric systems. The viscoelastic properties of these systems originate from the dynamics of a network comprising polymer molecules. The dynamic behavior of polymer solutions and their response to various flow conditions represent a cornerstone in the understanding of complex fluid mechanics. Our main objective is to develop constitutive equations for these systems at the mesoscale, particularly through the use of GPU-accelerated simulations and detailed modeling of polymer chain dynamics [1–5]. The advent of GPU computing has revolutionized the field of computational fluid dynamics by enabling large-scale simulations with significantly enhanced speed and efficiency. This approach allows for the exploration of complex fluid behaviors which were previously computationally prohibitive. GPU-accelerated simulations enable the analysis of large systems of non-interacting polymer chains, providing valuable insights into the microscale dynamics and their influence on the macroscale properties of the fluid.

RELATED RESEARCH WORK

Le Bris and Lelièvre [6] presented a comprehensive and technical exploration into the mathematical modelling of complex fluids, with a specific focus on polymeric fluids. In this work authors provided a detailed theoretical foundation for the study of Newtonian and non-Newtonian fluids, covering both fundamental aspects and advanced topics in fluid mechanics. This includes a comprehensive introduction to stochastic differential equations, the Monte Carlo method, Brownian motion, Itô calculus, and the Fokker Planck equation. The authors done an excellent job of illustrating the application of these stochastic methods in the context of fluid dynamics. In addition to the theoretical exploration, their work provided practical insights through the numerical simulation of a test case. This includes a discussion on the discretization of macroscopic equations, the handling of microscopic problems through deterministic and stochastic approaches, and the use of MATLAB codes.

In [7] Keunings presented a comprehensive analysis of the micro-macro approach, which seeks to connect the mesoscopic models of kinetic theory with the macroscopic continuum mechanics in fluid dynamics. The micro-macro approach operates on two levels. At the microscopic level, the behavior of individual molecules or molecular structures in the fluid is considered. Kinetic theory models are employed to represent these molecular configurations. Keunings discusses various models used at this level, like the Hookean and FENE dumbbell models for dilute polymer solutions and more advanced models for entangled polymer systems. These models account for the forces and interactions at the molecular level, including Brownian motion, elastic forces, and drag forces. On the macroscopic scale, the behavior of the fluid as a whole is considered. This involves solving the continuum mechanics conservation laws, which include the conservation of mass and momentum. The macroscopic properties, like flow velocity and stress fields, are determined by solving these equations. In this work Keunings also focuses on bridging these two scales through simulation techniques. The

micro-macro methods couple the molecular scale of kinetic theory with the macroscopic scale of continuum mechanics. This coupling is achieved through numerical techniques that solve the governing equations simultaneously. The microstructural models provide detailed insights into the molecular configurations, which in turn influence the macroscopic properties of the fluid. Keunings also shows how stochastic differential equations are used to describe the evolution of molecular configurations under the influence of random forces like Brownian motion. Monte Carlo methods are employed to simulate these stochastic processes, providing statistical information about molecular configurations. One of the challenges in implementing the micro-macro approach which Keunings discusses in his work is the high computational demand, which we are addressing in our work using GPU simulations.

In the study of polymeric fluid dynamics at the microscopic level, various models have been introduced to link microstructural movements with macroscopic responses, [as shown in Figure 1.1](#). Notably, bead-spring models stand out in this context. These models represent polymer chains through a simplified framework of beads linked by springs, a method known as molecular coarse-graining. Among the simplest of these is the elastic dumbbell model, which consists of a pair of beads. Despite its rudimentary nature, limiting its ability to fully capture the complexities of polymeric systems, this model is still valuable. It can adequately provide qualitative insights, particularly in describing the basic stretching and orientation behaviors of polymers, which are crucial in understanding their steady-state rheological properties and slow-moving flow dynamics [8].

The foundational models at the mesoscale, addressing breakage and reformation dynamics, were developed by Yamamoto [9], Tanaka and Edwards [10], Green and Tobolsky [11]. Various approaches have been taken in modeling wormlike micellar solutions. Van den Brule and Hoogerbrugge [12] developed a stochastic dumbbell model incorporating breaking and reforming processes, wherein the model specifi-

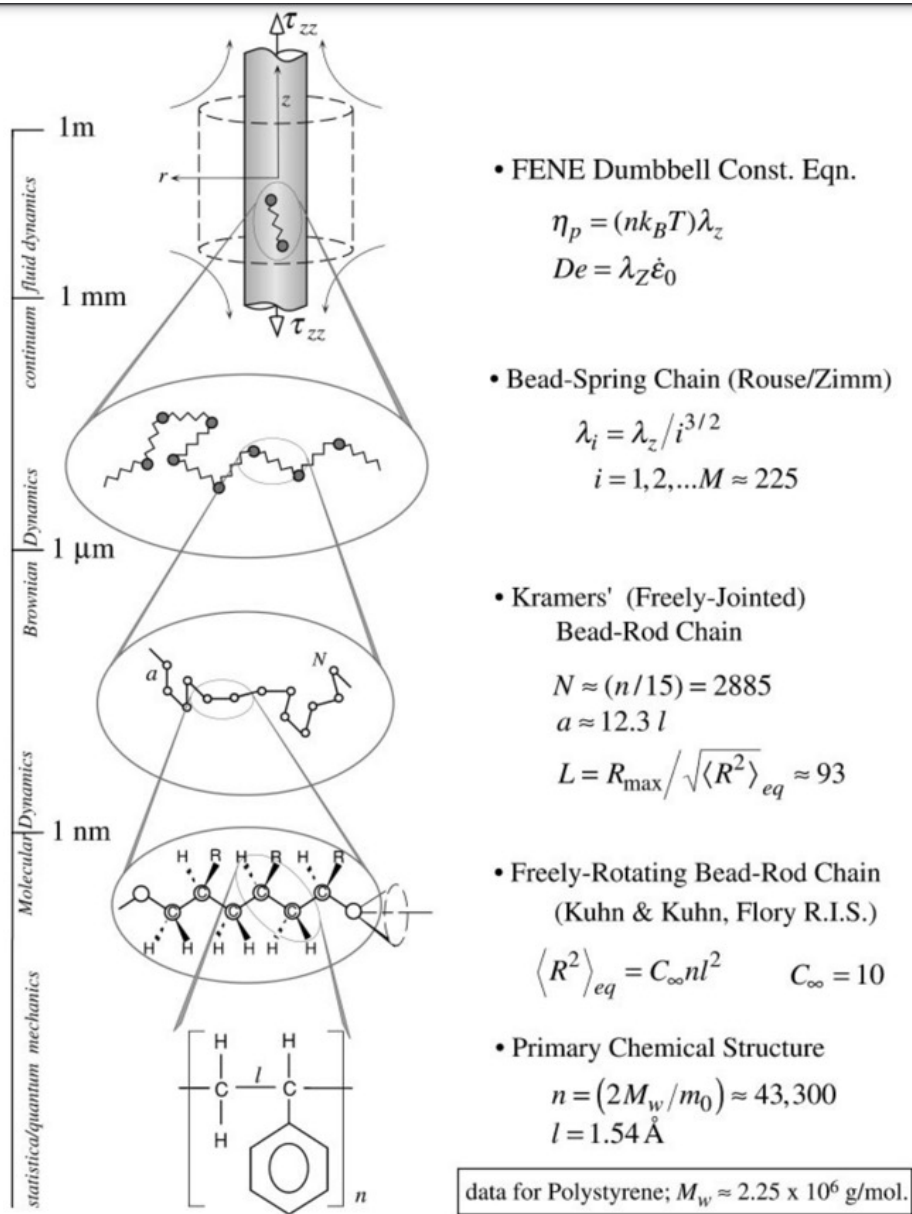


Figure 1.1 Coarse-grained representation of polymer molecules. Figure from [13]

cally tracks the topology of the dumbbells, including the position and connections of each bead or dumbbell. In their model beads were attaching to a node when they are within a certain fixed distance of that node. Vaccaro and Marrucci [14] introduced a model for transient networks formed by associating telechelic polymers, with

a focus on simple yet molecularly plausible kinetics for chain detachment and reattachment processes. In their work they focused on two structural components of the system: active chains that connect the network's nodes, and pendent chains that are temporarily disconnected at one end from the network with the assumption that the quantity of each chain type may vary during flow, but the total combined number of these chains remains constant. Rincón et. al. [15] presented a model analyzing the dynamics of transient networks in complex fluids, incorporating two kinetic processes and defining five microstates to represent macromolecular interactions within a Newtonian fluid. In [16] Vasquez, McKinley and Cook presented a network model (VCM) for wormlike micellar solutions, employing Cates' 'living polymer' theory, to explore the dynamics of chain scission and reformation under various flow conditions and examines the impact of model parameter variations on the solution's rheological behavior. In [17] Adams et al. enhanced VCM model for unentangled wormlike micelles by incorporating microscopic reversibility and spatial information about micelle breakage points. Park and Ianniruberto [18] introduced a new Brownian dynamics algorithm for telechelic polymers, focusing on understanding the rheological complexities of hydrophobically modified ethoxylated urethane solutions. In [19] Quintero et al. developed a stochastic mesoscale model simulating the breaking and reforming of single and double dumbbells. In their model they are tracking the topology and incorporating the dynamics of FENE springs. In [20] Cromer and Vasquez created a multiscale flow solver designed for GPUs, enabling highly efficient calculations. In their work they are utilizing a specific system with non-interacting dumbbells, which is inherently suited for parallelization.

The applications of these studies are vast and varied. For instance, the research on ink rheology by Hutchings et al. [21] and Guo et al. [22] has significant implications in the printing industry, particularly in improving the quality of inkjet printing and advancing 3D printing technologies. The study by Krishnan et al. [23] on complex

fluid rheology finds its applications in industries dealing with non-Newtonian fluids, including food, cosmetics, and pharmaceuticals. In the biomedical field, the work of Ulery et al. [24] on biodegradable polymers is instrumental for developing new drug delivery systems and biocompatible materials. The insights from Barbati et al. [25] on hydraulic fracturing have profound implications in the oil and gas industry. The research by Ewoldt and Saengow [26] on designing complex fluids has potential applications in consumer products, lubricants, and medical therapies.

CONTRIBUTIONS OF THIS DISSERTATION

In this study, we examine the stress response of fluids, particularly focusing on the distinction between Newtonian and viscoelastic materials. Newtonian fluids exhibit a linear relationship between stress and shear rate, encapsulated in the constitutive equation $\tau = \eta\dot{\gamma}$, where η represents viscosity. This equation highlights the uniformity in the stress response of Newtonian fluids, varying only in the viscosity coefficient across different materials. On the other hand, viscoelastic materials demonstrate a more intricate behavior as they lack a unified constitutive model due to their stress response's dependence on specific material properties and the nature of applied forces. This variability renders the study of viscoelastic materials both challenging and essential, given their prevalence in numerous industrial and biological applications. Our analysis extends to the dynamics of polymeric fluids, which are characterized by a microstructure consisting of polymer chains. These chains undergo various processes, such as twisting into coils or unwinding, forming cross-links by physically binding together. Their movement can be obstructed by getting entangled with each other or affected by the influence of neighboring polymer molecules these chains. **The new contribution from our work is the addition of stimuli-responsive dynamics. Stimuli-responsive materials refer to materials that can alter their rheological properties in response to external stimuli. Typically, this process involves the breaking and sub-**

sequent reformation of either network junctions or polymer chains. In this work, we focus mainly in breaking and reforming of the chains due to external flow fields. To adequately represent the dynamic processes of breaking and reforming of polymer chains, we utilize double dumbbells which are essentially composed of two single dumbbells that are physically interconnected.

In this work, we integrate GPU-accelerated simulations with our custom-designed stochastic modeling of breaking-reforming dynamics in polymer chains. Specifically, we advance the use of GPU computing for the simulation of complex fluids at the molecular level using non-interacting dumbbell models. This approach, inherently suitable for parallel computation, overcomes the computational limitations of previous traditional models, allowing for large-scale simulations that were not feasible before. Moreover, our approach not only enhances computational efficiency but also provides a more comprehensive picture of the intricate behaviors exhibited by these complex materials by integrating a double dumbbell breaking-reforming model instead of a single dumbbell model. These advances allow us to more accurately predict fluid behavior under a variety of conditions, thereby contributing to the advancement of technologies in various applied fields.

We divide this thesis into three main parts. In the first part we discuss two different representations at the mesoscale; namely Langevin and Fokker-Planck equations. In the second part, we discuss the formulation and solution of dumbbells models in viscometric flows, using GPU computing. The last part deals with the introduction of breaking and reforming dynamics to the dumbbell equations.

CHAPTER 2

COUPLING FLUID DYNAMICS USING LANGEVIN AND FOKKER-PLANCK EQUATIONS

This review focuses on two idealized scenarios involving microscopic particles embedded in a fluid. In the first one, we consider the uncoupled motion of individual Brownian probes, while in the second one, we consider the dynamics of an ensemble of such probes. These two cases allow us to explore the relation between two well-known families of equations in fluids dynamics: the Langevin equations (LE) and Fokker–Planck (FP) equations. By no means is this meant to be a comprehensive review of either of these equations, but rather a bird’s-eye view of their relationship and how they can be used to better understand fluid dynamics at the microscale. The article is written for undergraduate students and highlights different concepts from undergraduate courses in calculus and differential equations and their applications to fluid dynamics problems. In addition, whenever pertinent, the reader will be referred to more specialized publications for a more in-depth treatment of the different subjects.

To elucidate the relation between these two types of approaches, Figure 2.1 shows the relation between a LE and a FP description of particles moving as a result of simple Brownian motion in two dimensions. This process describes the random migration of small particles arising from their motion due to thermal energy. The term *Brownian motion* was coined after the botanist Robert Brown, who was the first to describe this phenomenon in 1828 during his investigation of the movements of fine

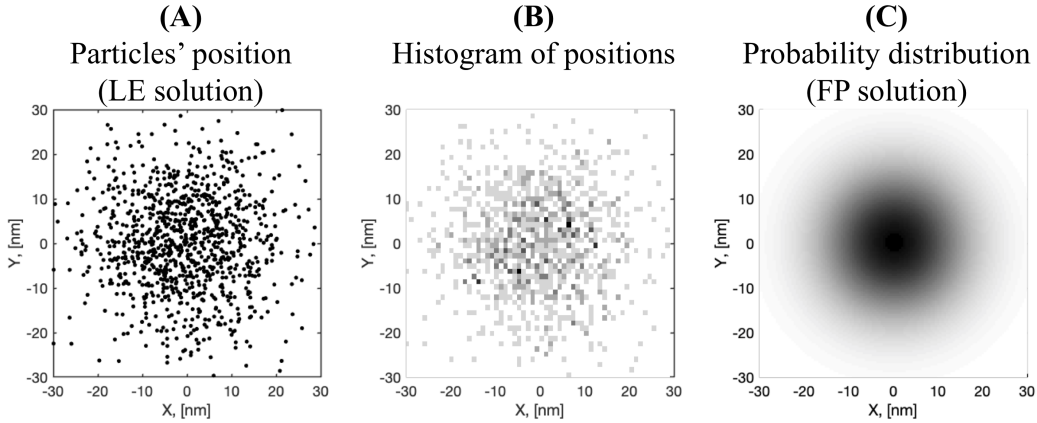


Figure 2.1 Relation between the Langevin equations (LE) and Fokker–Planck (FP) solutions. **(A)** LE solutions give particle positions as functions of time, each point represents a particle position at some time t . All particles have initial position $(0, 0)$ and follow different trajectories dictated by their respective noise history. **(B)** The distribution of particle positions can be summarized using a histogram. **(C)** FP solutions shows the probability of finding a particle at a given position as a function of time; darker color indicates a higher probability of finding a particle at that position.

particles, like pollen, dust, and soot, on a water surface. In 1905, Albert Einstein explained Brownian motion in terms of random thermal motions of fluid molecules bombarding the microscopic particle and causing it to undergo a random walk [33]. Nonetheless, the range of applications of Brownian motion goes beyond the study of microscopic particles and includes modeling of thermal noise, stock prices, and random perturbations in many physical, biological, and economic systems [34, 35]. From an observational point of view, the Langevin equation is easier to understand than the Fokker–Planck equation. The LE approach directly uses the concept of time evolution of the random variable describing the process; in the case of Figure 2.1, this corresponds to the individual particle’s position. In contrast, the FP approach follows the time evolution of the underlying probability distribution. That is, instead of describing a particle position, it describes the likelihood of finding a particle at a given position.

In this paper, we briefly describe the basics of LE equations and investigate their relation with their corresponding FP equations. The special cases discussed in the following sections are aimed at understanding how information is represented under these two different descriptions and illustrating how one can gather data under one approach and be able to infer behavior under the other.

2.1 LANGEVIN APPROACH

To understand the Langevin description, we start by considering a particle immersed in a fluid. The particle “feels” a force arising from the collisions with the fluid’s molecules. This force consists of two parts: (a) a deterministic hydrodynamic drag, which resists motion; and (b) a fluctuating stochastic force, caused by thermal fluctuations. Newton’s second law gives the evolution equation governing the dynamics of the particle as

$$\begin{aligned} m\mathbf{a} &= \sum \mathbf{F} \\ &= \text{drag force} + \text{random force.} \end{aligned}$$

Assuming a linear drag force (force = $-\text{drag coefficient} \times \text{velocity}$) and a white noise, the resulting equation is known as the Langevin equation:

$$m\mathbf{a} = m\dot{\mathbf{v}} = -\zeta\mathbf{v} + \mathbf{f}. \quad (2.1)$$

White noise describes a random term that assumes no correlation on the fluctuating forces; this is captured by drawing a random number from a Gaussian distribution with mean and variance given by

$$\langle \mathbf{f}(t) \rangle = \mathbf{0}, \quad (2.2a)$$

$$\langle f_i(t)f_j(s) \rangle = \Gamma\delta_{ij}\delta(t-s), \quad (2.2b)$$

where Γ represents the variance of the distribution or strength of the noise; i, j indicate vector components; δ_{ij} is the Kronecker delta; and $\delta(t)$ is a Dirac delta function. Note

that both the Kronecker delta and Dirac delta function capture the zero-correlation of the forces both spatial, $\delta_{ij} = 0$ for $i \neq j$, and temporal, $\delta(t - s) = 0$ for $t \neq s$. Moreover, for any interval $[a, b]$ contained in interval $[c, d]$, we have the following rule:

$$\int_a^b d\tau \int_c^d f(\tau, s) \delta(\tau - s) ds = \int_a^b f(\tau, \tau) d\tau \quad (2.3)$$

Since \mathbf{f} represents a stochastic term, Equation (2.1) is part of a broad class of differential equations known as stochastic differential equations (SDEs) [35, 36].

Assuming white noise, one can solve Equation (2.1) formally using basic solution techniques for ordinary differential equations (ODEs). In particular, Equation (2.1) can be treated as a first order, non-homogeneous differential equation of the form

$$\frac{dy(t)}{dt} + p(t)y(t) = q(t),$$

with integrating factor and solution given by

$$\nu(t) = \int p(t) dt, \quad y(t) = e^{-\nu(t)} \int e^{\nu(t)} q(t) dt.$$

For Equation (2.1), $y(t) = \mathbf{v}$, $p(t) = \zeta/m$ and $q(t) = \mathbf{f}$, so that its formal solution is given by

$$\begin{aligned} \mathbf{v}(t) &= \mathbf{v}(0)e^{-\zeta t/m} + \frac{1}{m} \int_0^t e^{-\zeta(t-\tau)/m} \mathbf{f}(\tau) d\tau \\ &= \mathbf{v}(0)e^{-t/\tau_B} + \frac{1}{m} \int_0^t e^{-(t-\tau)/\tau_B} \mathbf{f}(\tau) d\tau. \end{aligned} \quad (2.4)$$

The quantity $\tau_B = m/\zeta$ has units of time and is usually referred to as the Brownian relaxation time of the particle velocity.

Note that, in the absence of random noise, $\mathbf{f}(t) = 0$, Equation (2.4) gives $\mathbf{v}(t) = \mathbf{v}(0)e^{-t/\tau_B}$, which implies that $\mathbf{v} \rightarrow 0$ as $t \rightarrow \infty$. However, according to the equipartition theorem, the velocity should satisfy

$$\lim_{t \rightarrow \infty} \left\langle \frac{1}{2} m v^2(t) \right\rangle = \frac{d}{2} k_B T,$$

where the brackets $\langle \cdot \rangle$ represent averages; k_B is the Boltzmann's constant; T is the temperature; $v^2(t) = \mathbf{v}(t) \cdot \mathbf{v}(t)$; and d represents the degrees of freedom, or dimensionality, $d = 1, 2$ or 3 . The fact that the equipartition theorem states that the velocity cannot approach zero as time goes to infinity implies that the random force is necessary to obtain the correct equilibrium condition. Furthermore, the strength of the noise, Γ , should be such that equipartition theorem is satisfied.

To determine the strength of the random force, Γ , we take the average of $v^2(t)$ using Equation (2.4) as

$$\begin{aligned}
\langle \mathbf{v}(t) \cdot \mathbf{v}(t) \rangle &= \mathbf{v}(0) \cdot \mathbf{v}(0) e^{-2t/\tau_B} + \frac{2}{m} \int_0^t e^{-(2t-\tau)/\tau_B} [\mathbf{v}(0) \cdot \langle \mathbf{f}(t) \rangle] d\tau + \\
&\quad \frac{1}{m^2} \int_0^t \int_0^t e^{-(2t-\tau-s)/\tau_B} \langle \mathbf{f}(\tau) \cdot \mathbf{f}(s) \rangle d\tau ds, \\
\langle v^2(t) \rangle &= \mathbf{v}(0) \cdot \mathbf{v}(0) e^{-2t/\tau_B} + \frac{2}{m} \int_0^t e^{-(2t-\tau)/\tau_B} [0] d\tau \\
&\quad + \frac{d}{m^2} \int_0^t \int_0^t e^{-(2t-\tau-s)/\tau_B} [\Gamma \delta(\tau - s)] d\tau ds \\
&= v^2(0) e^{-2t/\tau_B} + \frac{d\Gamma}{2\zeta m} [1 - e^{-2t/\tau_B}]. \tag{2.5}
\end{aligned}$$

In the last step of Equation (2.5), we used the property of the Dirac delta function given in Equation (2.3). Taking the limit as $t \rightarrow \infty$ in Equation (2.5), and comparing it to the condition given by the equipartition theorem, gives

$$\begin{aligned}
\lim_{t \rightarrow \infty} \left\langle \frac{1}{2} m v^2(t) \right\rangle &= \frac{d}{2} k_B T && \text{Equipartition} \\
&= \frac{1}{2} m \left[\frac{d\Gamma}{2\zeta m} \right] = \frac{d\Gamma}{4\zeta} && \text{Equation (2.5)}.
\end{aligned}$$

Therefore, the strength of the noise should satisfy

$$\Gamma = 2 \zeta k_B T. \tag{2.6}$$

This relation between the strength of the fluctuations of the stochastic forces (Γ) and the dissipative term given by the drag force (ζ) is a special case of a more general result known as the *fluctuation–dissipation theorem* [37].

The fluctuation–dissipation theorem states that equilibrium is brought about by a dissipation force, in our case drag, between the particle and the medium, and whatever the mechanism of the dissipation, it has to be the same process that produces random, fluctuating forces on the particle. In other words, both the frictional force and the random force must be related since they have the same origin: fluid molecules “bombarding” the particle and inducing mobility.

Finally, after solving Equation (2.1), the particle position can be obtained as

$$\mathbf{x}(t) - \mathbf{x}(0) = \int_0^t \mathbf{v}(\tau) d\tau. \quad (2.7)$$

For a given SDE such as Equation (2.1), in order to make inferences based on its solution, it is necessary to find the average over many realizations. To illustrate this, consider the 2D version of Equation (2.1) solved three different times using the same initial position but subject to different random noises. The resulting trajectories are shown in Figure 2.2.

The fact that each trajectory is very different from the others implies that we cannot infer any behavior from the system by just considering a handful of solutions. That is, just as one would not be able to determine whether a coin is fair by just a couple of tosses, to be able to infer behavior based on Equation (2.1) one needs to look at many realizations of particle trajectories. This can be done numerically by solving the equation many times and then finding the average of such solutions or can be done analytically by using time-correlation functions, as discussed next.

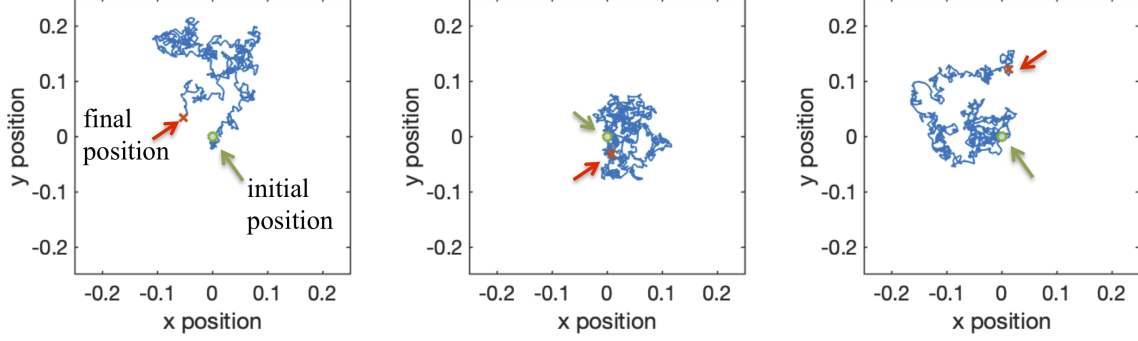


Figure 2.2 Evolution of 2D particle position for three different solutions of Equation (2.1). All three trajectories start from an initial position $(0, 0)$. In all three figures, $\Delta t = 0.001$ and the simulation ran for 1000 time steps.

2.1.1 MOMENTS OF A STOCHASTIC PROCESS

In mathematical statistics, the s^{th} moment of a set of stochastic observations $\{\mathbf{X}_i\}_{i=0}^n$ is defined as

$$M_s(\mathbf{X}) = \frac{1}{n} \sum_{i=1}^n \mathbf{X}_i^s.$$

Note that in the present application, our variables denote displacement of the particle with respect to the zero-time position, and the different moments measure deviations of the observations from the mean of the values. Within the context of fluid dynamics and Langevin equations, we are interested in the first ($s = 1$) and second ($s = 2$) moments of the particle positions. That is, the mean value of the stochastic variable and its spread or variance with respect to the mean.

- *First moment*

For the velocity in Equation (2.4), taking into account that $\langle \mathbf{f} \rangle = 0$, the mean is given by

$$M_1(\mathbf{v}) = \langle \mathbf{v}(t) \rangle = \mathbf{v}(0)e^{-t/\tau_B},$$

with a long-time or equilibrium value given by

$$M_1(\mathbf{v}) \rightarrow 0, \quad \text{as } t \rightarrow \infty.$$

For the particle position,

$$\begin{aligned}
M_1(\mathbf{x}) = \langle \mathbf{x} - \mathbf{x}(0) \rangle &= \int_0^t \langle \mathbf{v}(s) \rangle ds = \int_0^t \mathbf{v}(0) e^{-s/\tau_B} ds \\
&= -\mathbf{v}(0) \tau_B e^{-s/\tau_B} \Big|_0^t \\
&= \mathbf{v}(0) \tau_B \left[1 - e^{-t/\tau_B} \right].
\end{aligned}$$

In addition, its long-time behavior is

$$M_1(\mathbf{x}) \rightarrow \mathbf{v}(0) \tau_B, \quad \text{as } t \rightarrow \infty.$$

- *Second moment*

From Equation (2.5), the second moment for the velocity is

$$M_2(\mathbf{v}) = \langle v^2(t) \rangle = v^2(0) e^{-2t/\tau_B} + \frac{dk_B T}{m} \left[1 - e^{-2t/\tau_B} \right].$$

For the particle position, we have

$$\begin{aligned}
M_2(\mathbf{x}) &= \langle |\mathbf{x}(t) - \mathbf{x}(0)|^2 \rangle \\
&= \langle x^2(t) \rangle \\
&= \left\langle \left[\int_0^t v(\tau) d\tau \right]^2 \right\rangle \\
&= \left\langle \int_0^t \mathbf{v}(s) ds \cdot \int_0^t \mathbf{v}(\tau) d\tau \right\rangle \\
&= \int_0^t \int_0^t \langle \mathbf{v}(s) \cdot \mathbf{v}(\tau) \rangle d\tau ds \\
&= \int_0^t \int_0^t \left(v^2(0) e^{-\frac{s+\tau}{\tau_B}} + \frac{dk_B T}{m} \left[e^{-\frac{|s-\tau|}{\tau_B}} - e^{-\frac{s+\tau}{\tau_B}} \right] \right) d\tau ds \\
&= v^2(0) I_1 + \frac{dk_B T}{m} I_2 - \frac{dk_B T}{m} I_1.
\end{aligned}$$

In this derivation, we have again used Equation (2.3) and the properties of the Dirac-delta function. For clarity, we solve each integral separately:

$$\begin{aligned}
I_1 &= \int_0^t \int_0^t e^{-(s+\tau)/\tau_B} d\tau ds = \tau_B^2 \left(1 - e^{-t/\tau_B} \right)^2 \\
I_2 &= \int_0^t \int_0^t e^{-|s-\tau|/\tau_B} d\tau ds = 2 \int_0^t \int_0^s e^{-|s-\tau|/\tau_B} d\tau ds \\
&= 2\tau_B t - 2\tau_B^2 \left(1 - e^{-t/\tau_B} \right).
\end{aligned}$$

Substituting I_1 and I_2 into the equation for $M_2(\mathbf{x})$ gives

$$\begin{aligned}
\langle x^2(t) \rangle &= \left[v^2(0) - \frac{dk_B T}{m} \right] \left[\tau_B^2 (1 - e^{-t/\tau_B})^2 \right] \\
&\quad + \frac{dk_B T}{m} \left[2\tau_B t - 2\tau_B^2 (1 - e^{-t/\tau_B}) \right] \\
&= v^2(0)\tau_B^2 (1 - e^{-t/\tau_B})^2 \\
&\quad + \frac{dk_B T}{m} \tau_B^2 \left[- (1 - e^{-t/\tau_B})^2 + \frac{2}{\tau_B} t - 2 (1 - e^{-t/\tau_B}) \right] \\
&= v^2(0)\tau_B^2 (1 - e^{-t/\tau_B})^2 \\
&\quad + \frac{dk_B T}{m} \tau_B^2 \left[\frac{2}{\tau_B} t - 3 + 4e^{-t/\tau_B} - e^{-2t/\tau_B} \right]. \tag{2.8}
\end{aligned}$$

The quantity $\langle x^2(t) \rangle$ is called a mean squared displacement (MSD) and represents the square of the mean distance a particle has traveled in a given time interval. In practice, the MSD is one of the most commonly used experimental measures to determine material properties, as discussed in the next section.

2.1.2 APPLICATIONS OF THE MSD

Performing a Taylor expansion of the MSD about $t = 0$ gives

$$\langle x^2(t) \rangle \approx v^2(0) t^2 + O(t^3),$$

that is, at short times, the MSD grows quadratically in time. Similarly, at large times, we obtain

$$\langle x^2(t) \rangle \rightarrow \frac{2dk_B T}{m} \tau_B t, \quad \text{as } t \rightarrow \infty.$$

Using the definition of τ_B ,

$$\langle x^2(t) \rangle \rightarrow \frac{2dk_B T}{m} \frac{m}{\zeta} t = \frac{2dk_B T}{\zeta} t = 2dDt \quad \text{as } t \rightarrow \infty, \tag{2.9}$$

where we have introduced the *diffusion coefficient*, $D = k_B T / \zeta$.

The result in Equation (2.9) constitute a powerful tool in the characterization of fluids. The diffusion coefficient characterizes the mobility of particles of a given size in a given medium at a given temperature. For example, for spherical particles the drag

coefficient is given by $\zeta = 6\pi\eta a$, where a is the particle radius and η is the viscosity of the fluid. By embedding spherical particles in a fluid of unknown properties, one can estimate the viscosity of the fluid based on the particle trajectories.

Assume we had tracked the trajectories of n spherical particles diffusing in a Newtonian fluid, $\{\mathbf{x}_i(t)\}_{i=1}^n$, where $\mathbf{x}(t) = [x_i(t); y_i(t); z_i(t)]$. We can calculate the 1D, 2D, and 3D MSD as follows:

$$\begin{aligned} MSD_{1D}(\Delta t) &= \langle [x(t + \Delta t) - x(t)]^2 \rangle, \\ MSD_{2D}(\Delta t) &= \langle [x(t + \Delta t) - x(t)]^2 + [y(t + \Delta t) - y(t)]^2 \rangle, \\ MSD_{3D}(\Delta t) &= \langle [x(t + \Delta t) - x(t)]^2 + [y(t + \Delta t) - y(t)]^2 + [z(t + \Delta t) - z(t)]^2 \rangle. \end{aligned}$$

Examples of these MSDs are shown in Figure 2.3 for different Δt 's and the Matlab code used to generate them can be found in Appendix A. Note that in Appendix A we have used the zero-mass limit of the LE equation, see Section 2.1.4 for details of this limiting case.

Once the diffusion coefficient is found from the particle trajectories and the MSD, the fluid viscosity can be determined by

$$D = \frac{k_B T}{\zeta} = \frac{k_B T}{6\pi\eta a} \Rightarrow \eta = \frac{k_B T}{6\pi a D}. \quad (2.10)$$

This type of inference can also be used with more complex fluids and/or different types of particles. For instance, the Einstein–Smoluchowski–Sutherland relation states that [38]

$$D = \mu k_B T,$$

where μ is the particle's mobility. This mobility is given by Stokes' law in terms of the particle hydrodynamic radius, a_H ,

$$\mu = \frac{1}{c \pi \eta a_H},$$

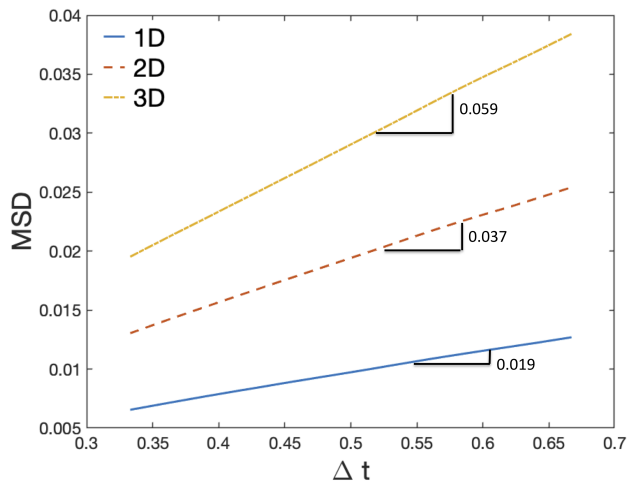


Figure 2.3 Mean squared displacement (MSD) in 1D, 2D, and 3D. Each line has been fitted to a function of the form $y = mx$, the best fitting value for the slope m is shown for each line. The slope for 1D is $2D = 0.019$, giving $D = 0.0095$, the slope for 2D gives $4D = 0.037 \Rightarrow D = 0.0093$, and for 3D it is $6D = 0.059 \Rightarrow D = 0.0098$. As a reference, the diffusion coefficient used to generate the particle trajectories is $D = 0.01$.

where both the constant c and a_H depend on the particle size and shape. Note that, for spherical particles, we return to the so called Stokes–Einstein relation,

$$D = \frac{k_B T}{6\pi\eta a},$$

however, the relation in Equation (2.10) stills holds for non-spherical particles.

In addition, complex fluids, such as viscoelastic materials, exhibit MSDs that do not depend linearly on time [39,40]. For example, the long-time MSD of some fluids obeys

$$MSD \sim t^\alpha.$$

This type of behavior is known as anomalous diffusion and the power law exponent, α , indicates the type of diffusion: for $\alpha < 1$, it is called subdiffusion, for $\alpha = 1$, regular diffusion, and for $\alpha > 1$, superdiffusion [41]. Although Equation (2.10) no longer holds in this case, material properties can still be inferred from the MSD of these fluids as discussed in [39,40].

2.1.3 GENERALIZED LANGEVIN EQUATIONS (GLE)

The GLE, as its name implies, is a generalization of Equation (2.1) and it can be similarly derived from Newton's second law assuming that the forces acting over the particle are a stochastic force, a drag force, and some external conservative force [35]:

$$m\ddot{\mathbf{x}}(t) = \mathbf{F}^R + \mathbf{F}^D + \mathbf{F}^E.$$

In the GLE approach, the drag coefficient is considered dynamic, so that the drag force is given by [37]

$$F^D = - \int_0^t K(t - \tau) \dot{\mathbf{x}}(\tau) d\tau,$$

where $K(t)$ is a memory kernel.

Since the external force is considered conservative, from Vector Calculus we know that this implies it arises from some potential field $V(\mathbf{x})$, such that

$$\mathbf{F}^E = -\nabla V(\mathbf{x}).$$

The resulting equation of motion is

$$m\ddot{\mathbf{x}}(t) = \mathbf{f}(t) - \int_0^t K(t - \tau) \dot{\mathbf{x}}(\tau) d\tau - \nabla V(\mathbf{x}). \quad (2.11)$$

The power of the GLE is that it is able to coarse-grain several degrees of freedom by describing: *(i)* explicitly the dynamics of variables of interests, which in this case corresponds to the position $\mathbf{x}(t)$ of a particle of mass m ; and *(ii)* implicitly the remaining degrees of freedom through a memory kernel $K(t)$, a random noise $\mathbf{f}(t)$, and an external potential $V(\mathbf{x})$. For free diffusion, particle mobility is in response *only* to stochastic thermal forces, i.e., $\nabla V(\mathbf{x}) \equiv \mathbf{0}$, but in more complex systems external forces also play a role, $\nabla V(\mathbf{x}) \neq \mathbf{0}$.

The memory kernel, $K(t)$, represents a retarded effect of the frictional force, and to generate the correct equilibrium statistics, the random noise has to be related to

this kernel in order to obey the fluctuation–dissipation theorem:

$$\langle f_i(t) f_j(s) \rangle = 2 k_B T \delta_{ij} K(t - s).$$

Physically, the kernel $K(t)$ represents the fact that the medium requires a finite time to respond to any fluctuations in the motion of the particle; this in turn affects how the medium acts back on the particle. Thus, the force that the medium exerts on the particle at a given time depends on what the particle did in the past.

For simple fluids and large Brownian particles, the medium is capable of responding infinitely quickly to changes in the particle position, i.e., it has no memory. In this case the memory kernel is a delta-function and Equation (2.11) reduces to the Langevin equation previously discussed [35, 37]:

$$K(t - \tau) = \zeta \delta(t - \tau) \tag{2.12}$$

$$m\ddot{\mathbf{x}}(t) = \mathbf{f}(t) - \zeta \dot{\mathbf{x}}(t) - \nabla V(\mathbf{x}). \tag{2.13}$$

Another extreme is a very sluggish medium that responds slowly to changes in the particle position. In this case, one can assume $K(t) \approx K(0) = K_0$, so that the GLE becomes

$$\begin{aligned} m\ddot{\mathbf{x}}(t) &= \mathbf{f}(t) - K_0 \int_0^t \dot{\mathbf{x}}(\tau) d\tau - \nabla V(\mathbf{x}) \\ &= \mathbf{f}(t) - K_0 (\mathbf{x}(t) - \mathbf{x}(0)) - \nabla V(\mathbf{x}) \\ &= \mathbf{f}(t) - \nabla \left(V(\mathbf{x}) + \frac{K_0}{2} \|\mathbf{x} - \mathbf{x}(0)\|^2 \right), \end{aligned} \tag{2.14}$$

thus adding an extra harmonic term to the potential. Such a term has the effect of trapping the system of particles in certain regions of its configuration space, an effect known as dynamic caging [42].

2.1.4 ZERO-MASS LIMIT OF THE LANGEVIN EQUATION

We finish this section on Langevin-type equations with a simplification. If we assume $K(t) = \zeta \delta(t)$, and that the particles are so small that their mass is negligible,

we obtain the so-called zero-mass limit:

$$0 = \mathbf{f}(t) - \zeta \dot{\mathbf{x}}(t) - \nabla V(\mathbf{x}).$$

This limit is also known as the *overdamped* or *inertialess limit* since it assumes that the inertial forces, $m\mathbf{a}$, are negligible compared to the other forces acting on the particle.

Rearranging terms and recalling that $\langle f_i(t) f_j(s) \rangle = 2 \zeta k_B T \delta_{ij} \delta(t - s)$ gives

$$\begin{aligned} \zeta \frac{d\mathbf{x}}{dt} &= -\nabla V(\mathbf{x}) + \mathbf{f}(t), \\ &= -\nabla V(\mathbf{x}) + \sqrt{2 \zeta k_B T} \mathbf{W}(t), \\ \frac{d\mathbf{x}}{dt} &= -\frac{1}{\zeta} \nabla V(\mathbf{x}) + \frac{1}{\zeta} \sqrt{2 \zeta k_B T} \mathbf{W}(t), \\ &= -\frac{1}{\zeta} \nabla V(\mathbf{x}) + \sqrt{\frac{2 k_B T}{\zeta}} \mathbf{W}(t), \\ \frac{d\mathbf{x}}{dt} &= -\frac{1}{\zeta} \nabla V(\mathbf{x}) + \sqrt{2 D} \mathbf{W}(t), \end{aligned} \tag{2.15}$$

where \mathbf{W} is a normally distributed random noise with $\langle \mathbf{W} \rangle = 0$ and $\langle W_i(t) W_j(s) \rangle = \delta_{ij} \delta(t - s)$. For simplicity, in the following sections, we only consider the relation between equations of the form (2.15) and their respective Fokker–Planck equations.

2.2 FOKKER–PLANCK APPROACH

As discussed in the previous section, when a system is described by an LE, a complete description of the macroscopic system will require the solution and averaging of *many* SDEs. An equivalent approach is to describe the system by macroscopic variables which fluctuate as a result of stochasticity, instead of describing the individual evolution of stochastic probes [43]. An excellent explanation of the different representations and their characteristics can be found in Risken’s book [43], which we summarize in Figure 2.4.

A Fokker–Planck (FP) equation is a partial differential equation that describes the evolution of the probability density function (PDF) of a stochastic variable.

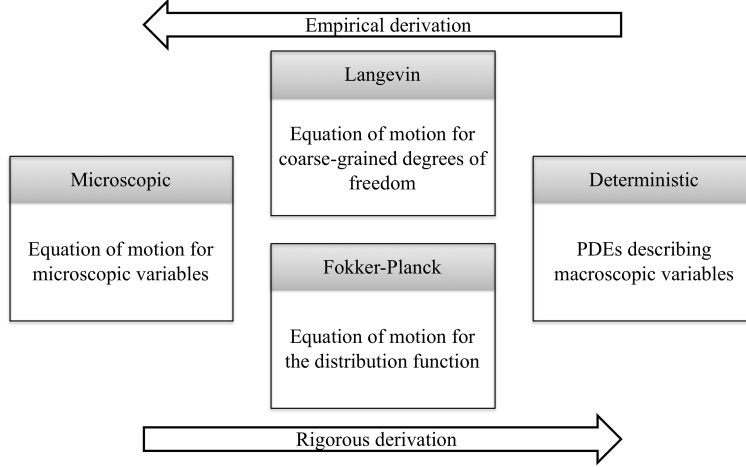


Figure 2.4 Levels of description of a system, adapted from [43].

For Langevin-type equations of the form given by Equation (2.15), the stochastic variable is a particle's position as a function of time, $\mathbf{x}(t)$. The corresponding PDF is the function that gives the probability of a particle being in the position \mathbf{x} at time t as $P(\mathbf{x}, t) d\mathbf{x}$. The reader is referred to Appendix B for a brief introduction to PDFs.

The LE equation given by Equation (2.15) can be written as

$$\begin{aligned} \frac{d\mathbf{x}}{dt} &= -\frac{1}{\zeta} \nabla V(\mathbf{x}) + \sqrt{2D} \mathbf{W}(t), \\ &= g_1(\mathbf{x}, t) + g_2(\mathbf{x}, t) \mathbf{W}(t), \end{aligned}$$

and the corresponding FP is given by [43],

$$\frac{\partial P}{\partial t} = -\nabla \cdot [g_1(\mathbf{x}, t) P(\mathbf{x}, t)] + \frac{1}{2} \nabla^2 [(g_2(\mathbf{x}, t))^2 P(\mathbf{x}, t)]. \quad (2.16)$$

Note that taking a *deterministic* perspective is equivalent to ignoring the random noise term in the LE, $g_2(\mathbf{x}, t) = 0$, which results in the absence of the diffusion term in the FP equation, $\nabla^2 [(\cdot) P(\mathbf{x}, t)]$. This simple statement helps us identify the relation between fluctuations at the microscale and diffusion at the macroscale. That is, the observed diffusion at the macroscale is the result of fluctuations arising from the fluid's molecules bombarding the probe at the microscale.

2.2.1 ONE-DIMENSIONAL EXAMPLES

In the following examples, we assume that all initial positions of particles are located at zero, that is,

$$\begin{aligned}x(0) &= 0 \\ P(x, 0) &= \delta(0).\end{aligned}$$

- *Brownian motion without external field for small particles ($m \rightarrow 0$)*

$$\frac{dx}{dt} = \sqrt{2D}W(t). \quad (2.17)$$

In this case, the corresponding FP equation is the well-known diffusion equation, which has the same mathematical form of the heat equation in the context of heat transfer under temperature gradients:

$$\begin{aligned}\frac{\partial P}{\partial t} &= -\frac{\partial}{\partial x} [0 \cdot P] + \frac{1}{2} \frac{\partial^2}{\partial x^2} [(\sqrt{2D})^2 P] \\ \frac{\partial P}{\partial t} &= D \frac{\partial^2 P}{\partial x^2}.\end{aligned} \quad (2.18)$$

We can find the general solution of this equation using similarity solutions with the transformation

$$P(x, t) = t^{-p} F(\mu), \quad (2.19)$$

where t^{-p} represents temporal decay and $\mu = x^2/(4Dt)$ is a shape factor used to reduce the partial differential equation (PDE) to an ordinary differential equation (ODE). For details on how this particular form is obtained, the reader is referred to [44].

We can calculate the derivatives of $P(x, t)$ using Equation (2.19) as

$$\frac{\partial P}{\partial t} = -pt^{-p-1} F(\mu) + t^{-p} \frac{dF}{d\mu} \frac{\partial \mu}{\partial t} = -pt^{-p-1} F(\mu) - \mu t^{-p-1} \frac{dF}{d\mu}$$

$$\frac{\partial P}{\partial x} = t^{-p} \frac{dF}{d\mu} \frac{\partial \mu}{\partial x} = \frac{x t^{-p-1}}{2D} \frac{dF}{d\mu}$$

$$\frac{\partial^2 P}{\partial x^2} = \frac{t^{-p-1}}{2D} \frac{dF}{d\mu} + \frac{x t^{-p-1}}{2D} \frac{d^2 F}{d\mu^2} \frac{\partial \mu}{\partial x} = \frac{t^{-p-1}}{2D} \frac{dF}{d\mu} + \frac{\mu t^{-p-1}}{D} \frac{d^2 F}{d\mu^2}$$

Substituting in Equation (2.18) gives

$$\begin{aligned} -pt^{-p-1} F(\mu) - \mu t^{-p-1} \frac{dF}{d\mu} &= D \left[\frac{t^{-p-1}}{2D} \frac{dF}{d\mu} + \frac{\mu t^{-p-1}}{D} \frac{d^2 F}{d\mu^2} \right] \\ \mu \frac{d}{d\mu} \left(\frac{dF}{d\mu} + F \right) + \frac{1}{2} \left(\frac{dF}{d\mu} + 2pF \right) &= 0. \end{aligned}$$

Since we have yet to define a value for p , we conveniently choose it to be $p = 1/2$, so that the two quantities in the parenthesis are the same. Finally, a solution for the resulting differential equation will satisfy

$$\frac{dF}{d\mu} + F = 0,$$

with the general solution

$$F(\mu) = C_0 e^{-\mu},$$

which gives the solution for $P(x, t)$,

$$P(x, t) = C_0 t^{-1/2} \exp\left(-\frac{x^2}{4Dt}\right).$$

To find the value of the constant of integration C_0 , we consider the fact that

$$\int_{-\infty}^{\infty} P(x, t) dx = 1,$$

that is, all possible realizations are included, see Appendix B.

To solve the integral, we introduce the error function $\text{erf}(y)$

$$\text{erf}(y) = \frac{2}{\sqrt{\pi}} \int_0^y e^{-s^2} ds$$

which has values $\text{erf}(-\infty) = -1$ and $\text{erf}(\infty) = 1$.

$$\begin{aligned} \int_{-\infty}^{\infty} P(x, t) dx &= \int_{-\infty}^{\infty} C_0 t^{-1/2} \exp\left(-\frac{x^2}{4Dt}\right) dx \\ &= C_0 t^{-1/2} \int_{-\infty}^{\infty} \exp\left(-\frac{x^2}{4Dt}\right) dx \\ &= C_0 t^{-1/2} \sqrt{\pi D t} \text{erf}\left(\frac{x}{2\sqrt{Dt}}\right) \Big|_{-\infty}^{\infty} \\ &= C_0 t^{-1/2} \sqrt{\pi D t} (2) = 2 C_0 \sqrt{\pi D}, \end{aligned}$$

which gives

$$C_0 = \frac{1}{2\sqrt{\pi D}} = \frac{1}{\sqrt{4\pi D}}.$$

Therefore, the solution of the FP equation is

$$P(x, t) = \frac{1}{\sqrt{4\pi D t}} \exp\left(-\frac{x^2}{4Dt}\right), \quad (2.20)$$

which is a one-dimensional Gaussian function centered at zero: $M_1(x) = 0$ and with variance $M_2(x) = 4Dt$.

To compare these results with those obtained in the LE section, we consider the first and second moments of $P(x, t)$.

The first moment is given by

$$\begin{aligned} M_1(x) &= \int_{-\infty}^{\infty} x P(x, t) dx \\ &= \int_{-\infty}^{\infty} x \frac{1}{\sqrt{4\pi D t}} \exp\left(-\frac{x^2}{4Dt}\right) dx \\ &= \frac{1}{\sqrt{4\pi D t}} \int_{-\infty}^{\infty} x \exp\left(-\frac{x^2}{4Dt}\right) dx. \end{aligned}$$

We use integration by substitution ($u = x^2$) to obtain

$$\begin{aligned}
\int x \exp\left(-\frac{x^2}{4Dt}\right) dx &= \int \frac{1}{2} \exp\left(-\frac{u}{4Dt}\right) du \\
&= -2Dt \exp\left(-\frac{u}{4Dt}\right) + C \\
&= -2Dt \exp\left(-\frac{x^2}{4Dt}\right) + C,
\end{aligned}$$

and

$$M_1(x) = \frac{1}{\sqrt{4\pi Dt}} \left[-2Dt \exp\left(-\frac{x^2}{4Dt}\right) \right]_{-\infty}^{\infty} = 0.$$

For the second moment, we have

$$\begin{aligned}
M_2(x) &= \int_{-\infty}^{\infty} x^2 P(x, t) dx \\
&= \int_{-\infty}^{\infty} x^2 \frac{1}{\sqrt{4\pi Dt}} \exp\left(-\frac{x^2}{4Dt}\right) dx \\
&= \frac{1}{\sqrt{4\pi Dt}} \int_{-\infty}^{\infty} x^2 \exp\left(-\frac{x^2}{4Dt}\right) dx \\
&= \frac{1}{\sqrt{4\pi Dt}} \left[-2x Dt \exp\left(-\frac{x^2}{4Dt}\right) \Big|_{-\infty}^{\infty} + \frac{(4Dt)^{3/2} \sqrt{\pi}}{4} \operatorname{erf}\left(\frac{x}{\sqrt{4Dt}}\right) \Big|_{-\infty}^{\infty} \right] \\
&= \frac{1}{\sqrt{4\pi Dt}} \left[0 + \frac{(4Dt)^{3/2} \sqrt{\pi}}{4} (2) \right] = \frac{1}{\sqrt{4\pi Dt}} \left[\frac{(4Dt)^{3/2} \sqrt{\pi}}{2} \sqrt{\pi} \right] \\
&= 2Dt,
\end{aligned}$$

which is the same result we obtained in the limit $t \rightarrow \infty$ for Equation (2.9), when the dimensionality is $d = 1$.

Solutions at different times are shown in Figure 2.5, together with the normalized histograms obtained from LE data. For details of the histogram normalization see Appendix B.

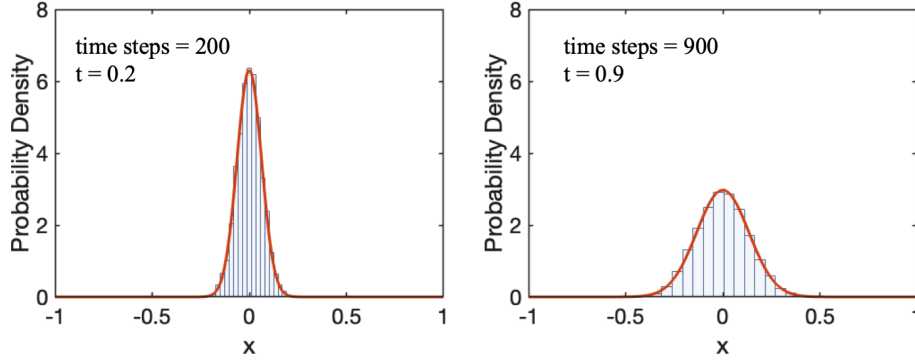


Figure 2.5 Probability density function (PDF) for position of particles diffusing via one-dimensional Brownian motion. Histograms correspond to LE data and solid lines corresponds to FP solutions. In this figure, $D = 10^{-2} \mu\text{m}^2/\text{s}$.

- *Brownian motion with external field for small particles ($m \rightarrow 0$)*

A common example of an external field is a background velocity, u , which imposes a drift on the particles:

$$\frac{dx}{dt} = u + \sqrt{2D}W(t). \quad (2.21)$$

The corresponding FP equation is the advection–diffusion equation

$$\begin{aligned} \frac{\partial P}{\partial t} &= -\frac{\partial}{\partial x} [u \cdot P] + \frac{1}{2} \frac{\partial^2}{\partial x^2} [(\sqrt{2D})^2 P] \\ \frac{\partial P}{\partial t} &= -u \frac{\partial P}{\partial x} + D \frac{\partial^2 P}{\partial x^2}. \end{aligned} \quad (2.22)$$

The solution of this PDE is [45]

$$P(x, t) = \frac{1}{\sqrt{4\pi Dt}} \exp\left(-\frac{(x - ut)^2}{4Dt}\right). \quad (2.23)$$

A comparison between Equations (2.20) and (2.23) shows that the only difference between these two solutions is in a “shift” of x by ut . That is, the effect of drift is to move the mean of the Gaussian distribution from zero.

As before we can calculate the first and second moment of the distribution

function as [45]

$$\begin{aligned}M_1(x) &= ut, \\M_2(x) &= u^2t^2 + 2Dt.\end{aligned}$$

That is, the mean position of the particle is displaced by the background velocity over a distance ut . In addition, note that the MSD at long times becomes $\sim t^2$ due to the additional *linear* flow in the fluid.

In the case of simple diffusion, the dispersion of the particles can be attained from the MSD or equivalently the variance of the Gaussian. In the case where drift is present, dispersion is superimposed by the background flow, for this reason a more accurate measure of the dispersion is given by the metric [45]

$$\sigma^2 = \int_{-\infty}^{\infty} (x - M_1(x))^2 P(x, t) dx = 2Dt,$$

which gives back the linear behavior characteristic of standard diffusive processes. Note that in this equation, $M_1(x)$ is a central moment as opposed to the general definition given at the beginning of Section 2.1.1. These two moments will coincide if the mean is zero.

Plots of Equation (2.23) are shown in Figure 2.6, where the solutions with drift are compared to solutions without drift.

2.2.2 TWO-DIMENSIONAL EXAMPLES

In this section, we present the 2D equations corresponding to four different cases and their numerical solutions.

- *No external field*

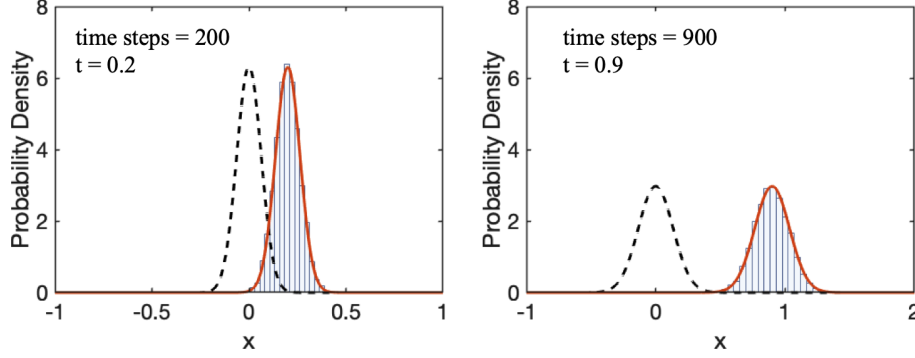


Figure 2.6 PDF for position of particles diffusing via one-dimensional Brownian motion plus drift. Histograms correspond to generalized Langevin equations (GLE) data and solid lines corresponds to FP solutions. For comparison, FP solutions without drift are shown in dashed lines. In this figure, $D = 10^{-2}\mu\text{m}^2/\text{s}$, $u = 0.2\mu/\text{s}$.

– Langevin equations

$$\begin{aligned}\frac{dx}{dt} &= \sqrt{2D}W_x(t), \\ \frac{dy}{dt} &= \sqrt{2D}W_y(t).\end{aligned}$$

In this case, both W_x and W_y are statistically independent white noises; the subscripts are used to denote that the noise histories are for x and y .

– Fokker–Planck Equation

$$\frac{\partial P}{\partial t} = D \left[\frac{\partial^2 P}{\partial x^2} + \frac{\partial^2 P}{\partial y^2} \right].$$

Solutions for LE and FP representations for this case of no external field are provided in Figure 2.7.

Note that, in two dimensions, we obtain two LEs, but still one FP equation. In general, as the degrees of freedom of the system increase, the choice between LE and FP representations is analogous to the choice between solving many SDEs and solving a single, high-dimensional PDE.

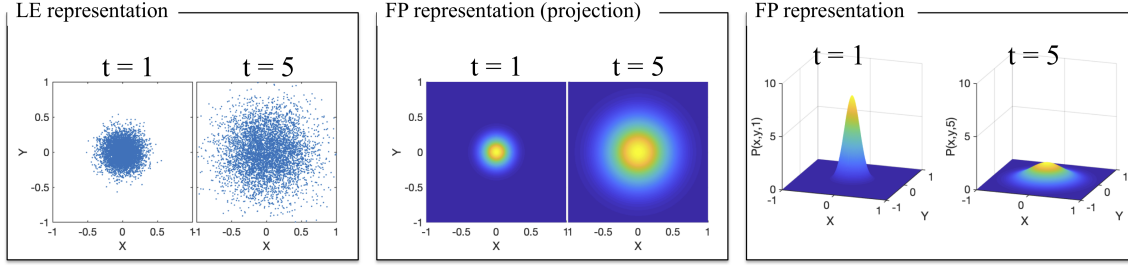


Figure 2.7 LE and FP solutions for two-dimensional Brownian motion without external field. For both representations, $D = 10^{-2} \mu\text{m}^2/\text{s}$ and time is in seconds. For the LE representation, the total number of particles is 5×10^3 .

- *Constant drift in the x-direction, $V(x, y) = u x$*

– Langevin equations

$$\begin{aligned}\frac{dx}{dt} &= u + \sqrt{2D}W_x(t), \\ \frac{dy}{dt} &= \sqrt{2D}W_y(t).\end{aligned}$$

– Fokker–Planck Equation

$$\frac{\partial P}{\partial t} = -u \frac{\partial P}{\partial x} + D \left[\frac{\partial^2 P}{\partial x^2} + \frac{\partial^2 P}{\partial y^2} \right].$$

Solutions for LE and FP representations for this case of constant drift in the x -direction are provided in Figure 2.8.

- *Background flow field, $\mathbf{u} = \mathbf{u}_0 + [u_x(x, y), u_y(x, y)]^T$*

For any background field of the form where u_0 and v_0 are constants,

$$\mathbf{u} = \begin{bmatrix} u_0 + u_x(x, y) \\ v_0 + u_y(x, y) \end{bmatrix},$$

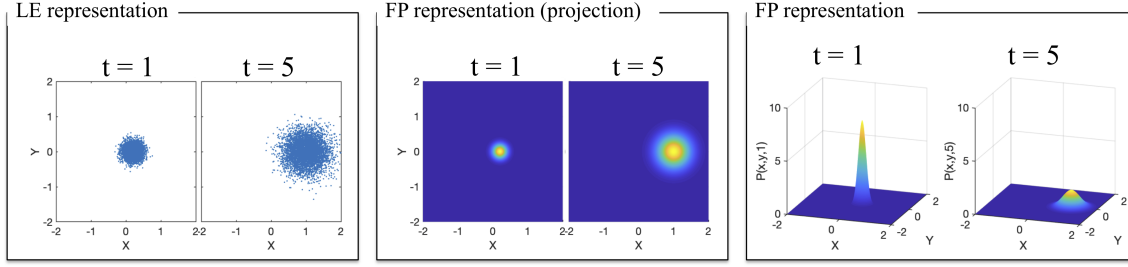


Figure 2.8 LE and FP solutions for two-dimensional Brownian motion with constant drift. For both representations, $D = 10^{-2} \mu\text{m}^2/\text{s}$, $u = 0.2 \mu/\text{s}$ and time is in seconds. For the LE representation, the total number of particles is 5×10^3 .

the Langevin equations are given by

$$\begin{aligned}\frac{dx}{dt} &= u_0 + \left(\frac{\partial u_x}{\partial x}\right)x + \left(\frac{\partial u_x}{\partial y}\right)y + \sqrt{2D}W_x(t), \\ \frac{dy}{dt} &= v_0 + \left(\frac{\partial u_y}{\partial x}\right)x + \left(\frac{\partial u_y}{\partial y}\right)y + \sqrt{2D}W_y(t).\end{aligned}$$

This equation can be written in vector form as

$$\frac{d\mathbf{x}}{dt} = \mathbf{u}_0 + \boldsymbol{\kappa} \cdot \mathbf{x} + \sqrt{2D}\mathbf{W},$$

where $\kappa_{ij} = \partial u_i / \partial x_j$ is the strain-rate tensor. The corresponding FP equation is

$$\frac{\partial P}{\partial t} = -\nabla \cdot [(\mathbf{u}_0 + \boldsymbol{\kappa} \cdot \mathbf{x}) P] + D \left[\frac{\partial^2 P}{\partial x^2} + \frac{\partial^2 P}{\partial y^2} \right].$$

Note that when $u_x = u_y = 0$, the equations reduce to those for constant drift, as discussed above.

– Example: simple shear, $\mathbf{u} = [U y, 0]^T$

$$\boldsymbol{\kappa} = \begin{bmatrix} \frac{\partial u_x}{\partial x} & \frac{\partial u_x}{\partial y} \\ \frac{\partial u_y}{\partial x} & \frac{\partial u_y}{\partial y} \end{bmatrix} = \begin{bmatrix} 0 & U \\ 0 & 0 \end{bmatrix}.$$

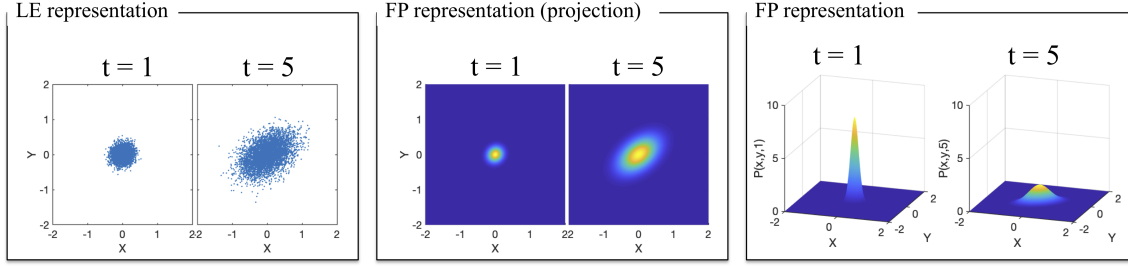


Figure 2.9 LE and FP solutions for two-dimensional Brownian motion with simple shear flow. For both representations, $D = 10^{-2} \mu\text{m}^2/\text{s}$, $U = 0.2 \mu/\text{s}$ and time is in seconds. For the LE representation, the total number of particles is 5×10^3 .

$$\boldsymbol{\kappa} \cdot \mathbf{x} = \begin{bmatrix} 0 & U \\ 0 & 0 \end{bmatrix} \cdot \begin{bmatrix} x \\ y \end{bmatrix} = \begin{bmatrix} U y \\ 0 \end{bmatrix}.$$

$$\nabla \cdot [(\boldsymbol{\kappa} \cdot \mathbf{x}) P] = \begin{bmatrix} \frac{\partial}{\partial x} \\ \frac{\partial}{\partial y} \end{bmatrix} \cdot \begin{bmatrix} U y P \\ 0 \end{bmatrix} = \begin{bmatrix} U y \frac{\partial P}{\partial x} \\ 0 \end{bmatrix}.$$

* Langevin equations

$$\begin{aligned} \frac{dx}{dt} &= U y + \sqrt{2D} W_x(t), \\ \frac{dy}{dt} &= \sqrt{2D} W_y(t). \end{aligned}$$

* Fokker–Planck Equation

$$\frac{\partial P}{\partial t} = -U y \frac{\partial P}{\partial x} + D \left[\frac{\partial^2 P}{\partial x^2} + \frac{\partial^2 P}{\partial y^2} \right].$$

Solutions for LE and FP representations for this case of simple shear flow are provided in Figure 2.9.

CHAPTER 3

MICRO-MACRO DESCRIPTIONS OF VISCOELASTIC MATERIALS

3.1 CONSERVATION EQUATIONS

In the study of viscoelastic fluid dynamics, particularly under unsteady and incompressible conditions, and in the absence of external forces, two primary conservation principles govern the flow: mass and momentum.

The conservation of mass is governed by the continuity equation, which asserts the constancy of mass in a fluid flow. It is mathematically expressed as:

$$\nabla \cdot \tilde{\mathbf{u}} = 0 \quad (3.1)$$

where $\tilde{\mathbf{u}}$ represents the dimensional velocity vector of the fluid. This equation implies that the fluid's mass is neither generated nor annihilated within the flow field.

The conservation of momentum, accounting for viscoelastic effects, extends the classic Navier-Stokes equation. It includes terms for inertial forces, pressure gradients, solvent viscosity, and viscoelastic stresses. The dimensional form of the conservation of momentum is given by:

$$\rho \left(\frac{\partial \tilde{\mathbf{u}}}{\partial t} + \tilde{\mathbf{u}} \cdot \nabla \tilde{\mathbf{u}} \right) = -\nabla \tilde{p} + \tilde{\eta}_s \nabla^2 \tilde{\mathbf{u}} + \nabla \cdot \tilde{\boldsymbol{\tau}} \quad (3.2)$$

where $\tilde{\rho}$ is the fluid density, \tilde{p} is the pressure, $\tilde{\eta}_s$ is the solvent viscosity, and $\tilde{\boldsymbol{\tau}}$ is the extra stress tensor.

For non-dimensionalization, the equations are scaled using characteristic macroscopic scales such as a length scale L , a velocity scale U , the zero shear rate polymeric viscosity η_p , and the longest relaxation time λ . The relationships between dimensional and non-dimensional parameters are defined as follows [20]:

$$t = \tilde{t} \cdot \left(\frac{U}{L}\right), \quad \mathbf{x} = \tilde{\mathbf{x}} \cdot \left(\frac{1}{L}\right), \quad \mathbf{u} = \tilde{\mathbf{u}} \cdot \left(\frac{1}{U}\right), \quad p = \tilde{p} \cdot \left(\frac{1}{\rho U^2}\right), \quad \boldsymbol{\tau} = \tilde{\boldsymbol{\tau}} \cdot \left(\frac{\lambda}{\eta_p}\right). \quad (3.3)$$

The non-dimensional forms of the equations are then:

$$\nabla \cdot \mathbf{u} = 0, \quad (3.4)$$

$$\frac{\partial \mathbf{u}}{\partial t} + \mathbf{u} \cdot \nabla \mathbf{u} = -\nabla p + \frac{\beta}{Re} \nabla^2 \mathbf{u} + \frac{1-\beta}{Re De} \nabla \cdot \boldsymbol{\tau} \quad (3.5)$$

Here, $Re = \frac{\rho U L}{\eta}$ and $De = \frac{\lambda U}{L}$ are the Reynolds and Deborah numbers, respectively, representing the ratio of inertial to viscous forces and the fluid's relaxation time to the characteristic flow time. The parameter $\beta = \frac{\eta_s}{\eta_s + \eta_p}$ is the ratio of solvent viscosity to total zero-shear viscosity.

3.2 CONSTITUTIVE MODELING USING DUMBBELLS REPRESENTATIONS

On the micro level we begin with the position vectors r_i of a free bead or a junction of 2 beads within an fixed chain of $N-1$ dumbbells (Fig.3.1). The motion of these vectors is subject to a balance of several forces: the force exerted by the spring, the hydrodynamic drag, and the Brownian motion force. To ensure accurate representation of drag forces in the model, the drag coefficient assigned to a single, free bead is denoted as ζ . In contrast, at the junctions, which are the meeting points of two beads, the drag coefficient effectively becomes 2ζ . This adjustment accounts for the cumulative drag experienced by two interconnected beads, compared to the drag on an individual, isolated bead.

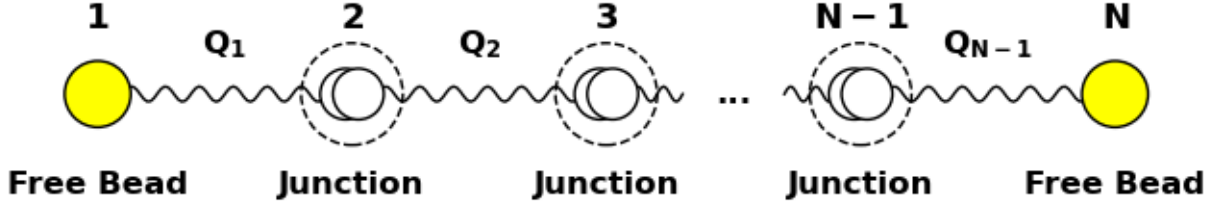


Figure 3.1 Dumbbell chain configuration composed of $N - 1$ merged dumbbells.

3.2.1 SINGLE DUMBBELL REPRESENTATION

We start with a case of a single dumbbell as shown in Figure 3.2.

Here we assume homogeneous flow conditions, so the motions of the beads are described by a Langevin equation [27]:

$$\frac{d\tilde{\mathbf{r}}_1}{dt} = (\tilde{\nabla}\tilde{\mathbf{u}})^T \cdot \tilde{\mathbf{r}}_1 - \frac{1}{\zeta}\mathbf{F}(\tilde{\mathbf{r}}_{1,2}) + \sqrt{\frac{2k_B T}{\zeta}}\mathbf{f}_1, \quad (3.6)$$

$$\frac{d\tilde{\mathbf{r}}_2}{dt} = (\tilde{\nabla}\tilde{\mathbf{u}})^T \cdot \tilde{\mathbf{r}}_2 - \frac{1}{\zeta}\mathbf{F}(\tilde{\mathbf{r}}_{2,1}) + \sqrt{\frac{2k_B T}{\zeta}}\mathbf{f}_2. \quad (3.7)$$

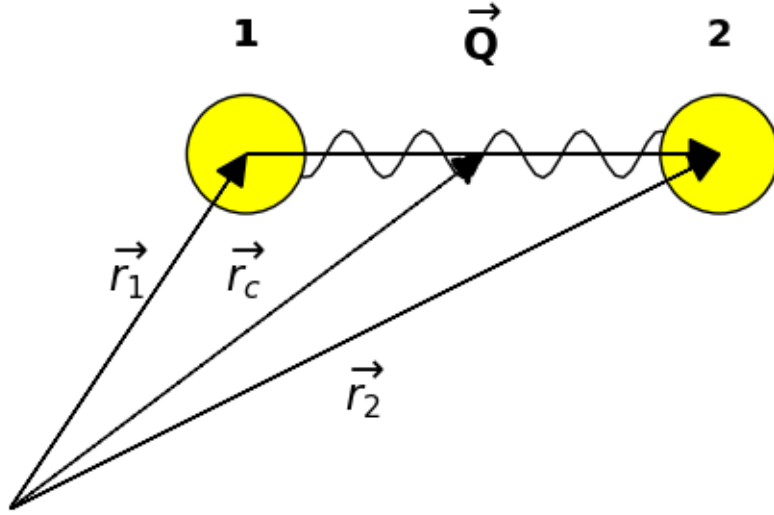


Figure 3.2 Single dumbbell configuration given by the coordinates of each dumbbell, \vec{r}_1 and \vec{r}_2 , or its center of mass, \vec{r}_c and end-to-end vector, \vec{Q} .

Here \mathbf{u} is the velocity vector of the flow, $\mathbf{F}(\mathbf{r}_{i,j})$ denotes the function of the spring force acting on the bead i due to its connection with bead j , ζ is the drag coefficient, $k_B T$ represents the thermal energy, where k_B is the Boltzmann constant and T is the temperature, and $\mathbf{f} = [f_1, f_2]^T$ is a Brownian force, with mean and variance given by

$$\langle \mathbf{f}(t) \rangle = \mathbf{0}, \quad (3.8a)$$

$$\langle f_1(t) f_2(s) \rangle = \delta_{12} \delta(t - s). \quad (3.8b)$$

In the methodology employed for our GPU-based approach, we operate under the premise of a homogeneous distribution. This framework negates the necessity to monitor the spatial positions of the dumbbells. Instead of solving system of equations for position vectors \mathbf{r}_i , for each dumbbell in the chain we introduce its center of mass $\mathbf{r}_i^c = \frac{1}{2}(\mathbf{r}_i + \mathbf{r}_{i+1})$, $i = 1, \dots, N - 1$ and the end-to-end connector vector $\mathbf{Q}_i = \mathbf{r}_{i+1} - \mathbf{r}_i$ (Fig. 3.2). Due to the homogeneous assumptions in our model, equations for \mathbf{r}_i^c are

not required. Our focus is primarily on \mathbf{Q}_i , and here is the resulting equation, which we get from Eqns. (3.6)-(3.7):

$$\frac{d\tilde{\mathbf{Q}}}{dt} = (\tilde{\nabla}\tilde{\mathbf{u}})^T \cdot \mathbf{Q} - \frac{1}{\zeta}(\mathbf{F}(\tilde{\mathbf{r}}_{2,1}) - \mathbf{F}(\tilde{\mathbf{r}}_{1,2})) + \sqrt{\frac{2k_B T}{\zeta}}(\mathbf{f}_2 - \mathbf{f}_1), \quad (3.9)$$

which can be simplified to:

$$\frac{d\tilde{\mathbf{Q}}}{dt} = (\tilde{\nabla}\tilde{\mathbf{u}})^T \cdot \tilde{\mathbf{Q}} - \frac{2}{\zeta}\mathbf{F}(\tilde{\mathbf{Q}}) + \sqrt{\frac{2k_B T}{\zeta}}d\mathbf{W}_t, \quad (3.10)$$

where \mathbf{W}_t is a Wiener process sampled from a normal distribution with a mean of **zero** and a variance of dt .

There are several approaches to obtain viscoelastic stresses from the moments of the end-to-end vector \mathbf{Q} . Here we use Kramer's formula [8]:

$$\tilde{\boldsymbol{\tau}} = n\langle F(\tilde{\mathbf{Q}})\tilde{\mathbf{Q}} \rangle - nk_B T \mathbf{I}, \quad (3.11)$$

where $\boldsymbol{\tau}$ is the stress tensor, n is the dumbbells number density, $n\langle F(\tilde{\mathbf{Q}})\tilde{\mathbf{Q}} \rangle$ accounts for the force exerted by the spring, which follows the spring force $F(\tilde{\mathbf{Q}})$, $nk_B T$ reflects the influence of the Brownian motion, and \mathbf{I} is the 3×3 identity matrix.

The final step consists on defining the functional form for the spring force, $F(\tilde{\mathbf{Q}})$. Below we discuss two approaches.

3.2.2 HOOKEAN SPRING LAW

In the Hookean model, the force $F(Q_j)$ is assumed to follow Hooke's law, which is a linear elastic law,

$$F(\tilde{\mathbf{Q}}) = H\tilde{\mathbf{Q}}, \quad (3.12)$$

where H is the spring constant. This model simplifies the complex dynamics of polymer chains by considering the force to be directly proportional to the distance between the beads.

Applying Hookean force, we can rewrite Eqns. (3.10) and (3.11) as follows:

$$\frac{d\tilde{\mathbf{Q}}}{dt} = (\tilde{\nabla}\tilde{u})^T \cdot \tilde{\mathbf{Q}} - \frac{2H}{\zeta} \tilde{\mathbf{Q}} + \sqrt{\frac{4k_B T}{\zeta}} dW_t, \quad (3.13)$$

$$\tilde{\boldsymbol{\tau}} = nH \langle \tilde{\mathbf{Q}}\tilde{\mathbf{Q}} \rangle - nk_B T \mathbf{I}. \quad (3.14)$$

To get non-dimensional equations, we are using same relations as in Eqn. (3.3) and the characteristic microscopic length,

$$x = \sqrt{\frac{k_B T}{H}}. \quad (3.15)$$

The non-dimensional parameters are related to their dimensional counterparts by:

$$\eta_p = nk_B T \lambda, \quad (3.16)$$

$$\tau = \tilde{\tau} \left(\frac{\lambda}{\eta_p} \right) = \tilde{\tau} \left(\frac{1}{nk_B T} \right), \quad (3.17)$$

$$Q = \tilde{Q} \cdot \sqrt{\frac{H}{k_B T}}. \quad (3.18)$$

Lastly, the system's longest relaxation time, indicating the time for the dumbbell to reach equilibrium after disturbance, is defined as:

$$\lambda = \frac{\zeta}{4H}. \quad (3.19)$$

Using this relations, non-dimensional equations for a Hookean single dumbbell then read:

$$\frac{d\mathbf{Q}}{dt} = (\nabla u)^T \cdot \mathbf{Q} - \frac{1}{2De} \mathbf{Q} + \frac{1}{\sqrt{De}} dW_t, \quad (3.20)$$

$$\boldsymbol{\tau} = \langle \mathbf{Q}\mathbf{Q} \rangle - \mathbf{I}. \quad (3.21)$$

3.2.3 FENE [SPRING LAW](#)

In the case of a FENE (Finitely Extensible Nonlinear Elastic) model, the spring force is given by a non-linear equation to account for the finite extensibility of polymer chains. The force equation is [8]:

$$F(\tilde{\mathbf{Q}}) = \frac{H\tilde{\mathbf{Q}}}{1 - (\tilde{Q}/Q_{\max})^2} \quad (3.22)$$

where $\tilde{Q}^2 = \tilde{\mathbf{Q}} \cdot \tilde{\mathbf{Q}}$ and Q_{\max} is the maximum extension of the spring. This model is more realistic for simulating polymer behavior under large deformations.

For a single dumbbell under the FENE force, the equations corresponding to Eqns. (3.10) and (3.11) become:

$$\frac{d\tilde{\mathbf{Q}}}{dt} = (\tilde{\nabla}\tilde{u})^T \cdot \tilde{\mathbf{Q}} - \frac{2H}{\zeta} \left(\frac{\tilde{\mathbf{Q}}}{1 - (\tilde{Q}_t/Q_{\max})^2} \right) + \sqrt{\frac{4k_B T}{\zeta}} dW_t, \quad (3.23)$$

$$\tilde{\boldsymbol{\tau}} = nH \left\langle \frac{\tilde{\mathbf{Q}}\tilde{\mathbf{Q}}}{1 - (\tilde{Q}/Q_{\max})^2} \right\rangle - nk_B T \mathbf{I}. \quad (3.24)$$

The non-dimensional parameters and relations remain as described in the Hookean case, with an additional non-dimensional nonlinear FENE parameter:

$$b = H Q_{\max}^2 / (k_B T). \quad (3.25)$$

Thus, the non-dimensional FENE equations for a single dumbbell are:

$$\frac{d\mathbf{Q}}{dt} = (\nabla u)^T \cdot \mathbf{Q} - \frac{1}{2De} \left(\frac{\mathbf{Q}}{1 - Q_t^2/b} \right) + \frac{1}{\sqrt{De}} dW_t, \quad (3.26)$$

$$\boldsymbol{\tau} = \left\langle \frac{\mathbf{Q}\mathbf{Q}}{1 - Q^2/b} \right\rangle - \mathbf{I}. \quad (3.27)$$

3.3 NUMERICAL SCHEMES

In our approach, each GPU thread is responsible for dynamics of one dumbbell. During its evolution, dumbbell can change its type between single and double, while being calculated completely on one thread without any interactions with other threads. From this set up it can be seen that the amount of dumbbells remains constant and is equal to the number of running threads, while the number of beads is changing. Implementing the numerical schemes presented unique challenges, particularly in optimizing GPU thread utilization for individual dumbbell dynamics. The process required careful balancing to maximize computational efficiency while maintaining accuracy, highlighting the complexities of parallel computation in simulating intricate fluid behaviors.

Each dt_{macro} step, values from all threads are sent from the GPU to the CPU to be saved. In future iterations of this work, there is potential to explore more sophisticated data transfer and management techniques between GPU and CPU, aiming to minimize data transmission time and optimize memory usage. Additionally, the integration of emerging parallel processing architectures could further enhance the simulation efficiency, enabling the exploration of even larger and more complex systems.

3.3.1 INITIALIZATION STEPS

At the beginning of the simulation, the system parameters and variables are initialized. This includes setting up the number of threads (dumbbells), Deborah number De , maximum spring extension (b), deformation tensor (κ) and three time steps ($dt_{\text{macro}}, dt_{\text{prob}}, dt_{\text{micro}}$).

3.3.2 HOOKEAN DUMBBELLS EVOLUTION

In the case of Hookean Dumbbells, we are using a forward Euler scheme. For each single dumbbell we solve corresponding evolution Eqn.(3.20):

$$\mathbf{Q}(t_{j+1}) = \mathbf{Q}(t_j) + \left[(\nabla \mathbf{u})^T \cdot \mathbf{Q}(t_j) - \frac{1}{2De} \mathbf{Q}(t_j) \right] \Delta t_j + \frac{1}{\sqrt{De}} \Delta \mathbf{W}_j. \quad (3.28)$$

3.3.3 FENE DUMBBELLS EVOLUTION

In the case of FENE Dumbbells due to the introduction of non-linearity in the evolution equation, a semi-implicit algorithm of the first order is employed instead of the forward Euler scheme.

PREDICTOR STEP

The predictor step computes an intermediate **connector vector** \mathbf{S} for each dumbbell [27,30]:

$$\mathbf{S} = \mathbf{Q}(t_j) + \left[(\nabla \mathbf{u})^T \cdot \mathbf{Q}(t_j) - \frac{F(\mathbf{Q}(t_j))}{2De} \right] \Delta t_j + \sqrt{\frac{1}{De}} \Delta \mathbf{W}_j \quad (3.29)$$

where $\mathbf{Q}(t_j)$ is the **current end-to-end connector** vector, $F(\mathbf{Q}(t_j))$ is related to the FENE spring force and we define it as:

$$F(\mathbf{Q}(t_j)) = \frac{\mathbf{Q}(t_j)}{1 - Q(t_j)^2/b}, \quad (3.30)$$

CORRECTOR STEP

The corrector step refines the **connector vector** based on the predictor step:

$$\begin{aligned} \mathbf{Q}(t_{j+1}) \left[1 + \frac{1}{4De} \frac{\Delta t_j}{1 - Q^2(t_{j+1})/b} \right] = & \mathbf{Q}(t_j) + \sqrt{\frac{1}{De}} \Delta \mathbf{W}_j \\ & + \frac{\Delta t_j}{2} \left[(\nabla \mathbf{u})^T \cdot \mathbf{S} + (\nabla \mathbf{u})^T \cdot \mathbf{Q}(t_j) \right] \\ & - \frac{\Delta t_j F(\mathbf{Q}(t_j))}{4De}, \end{aligned} \quad (3.31)$$

CUBIC EQUATION

To get [new end-to-end connector vector](#) from the previous corrector step, we need to solve the following cubic equation, which has a unique real solution in $(0, \sqrt{b})$ [31]:

$$x^3 - Px^2 - b \left(1 + \frac{1}{4De} \Delta t_j \right) x + bP = 0, \quad (3.32)$$

where \mathbf{P} is the the right-hand-side of the previous [corrector step Eqn. \(3.31\)](#) and P is the magnitude of \mathbf{P} .

POSITION UPDATE

The new end-to-end connector vector of each dumbbell is updated according to the following formula:

$$\mathbf{Q}(t_{j+1}) = x \cdot \frac{\mathbf{P}}{P}. \quad (3.33)$$

3.4 MACROSCOPIC CLOSURES OF DUMBBELL MODELS

Here, we present macroscopic closure models for the Hookean and FENE dumbbell configurations discussed in Section 3.2. We use these macroscopic models to compare with their corresponding microscopic counterparts with the key aim to investigate the degree of microscale detail that is potentially lost when using macroscopic closures. This comparison is crucial to demonstrate the limitations of macroscopic models and to highlight the vital role of integrating micro-macro modeling techniques. Using Eqn. (3.10) we obtain an equation for the second moment of the end-to-end vector \mathbf{Q} ,

$$\left(\langle\langle\tilde{\mathbf{Q}}\tilde{\mathbf{Q}}\rangle\rangle\right)_{(1)} + \frac{4}{\zeta} \langle F(\tilde{\mathbf{Q}})\tilde{\mathbf{Q}} \rangle = \frac{4k_B T}{\zeta} \mathbf{I}, \quad (3.34)$$

where $(\cdot)_{(1)}$ represents the upper convected derivative of (\cdot) , defined as:

$$(\cdot)_{(1)} = \frac{\partial(\cdot)}{\partial t} + \mathbf{u} \cdot \nabla(\cdot) - (\cdot) \cdot (\nabla \mathbf{u}) - (\nabla \mathbf{u})^T \cdot (\cdot). \quad (3.35)$$

3.4.1 HOOKEAN DUMBBELLS

The Hookean dumbbell model, utilizing a linear spring force, leads to the well-known Upper Convected Maxwell (UCM) model. The non-dimensionalized stress tensor and evolution equations are:

$$\boldsymbol{\tau} = \langle \mathbf{Q}\mathbf{Q} \rangle - \mathbf{I} \quad (3.36)$$

$$De(\langle \mathbf{Q}\mathbf{Q} \rangle)_{(1)} + \langle \mathbf{Q}\mathbf{Q} \rangle = \mathbf{I} \quad (3.37)$$

3.4.2 FENE DUMBBELLS

The FENE model, representing finite extensibility, yields different closures [29]. In our work we use FENE-P model for which the non-dimensionalized constitutive equations are [20]:

$$\boldsymbol{\tau} = \frac{\langle \mathbf{Q}\mathbf{Q} \rangle}{1 - \langle Q^2 \rangle / b} - \mathbf{I} \quad (3.38)$$

$$De(\langle \mathbf{Q}\mathbf{Q} \rangle)_{(1)} + \frac{\langle \mathbf{Q}\mathbf{Q} \rangle}{1 - \langle Q^2 \rangle / b} = \mathbf{I} \quad (3.39)$$

3.5 RESULTS

We present our results for a case of a simple shear flow, which is created by positioning a fluid between two parallel plates, where the bottom plate remains fixed and the top plate moves at a constant speed, denoted by U_{top} . The results for the simple shear flow case lay the foundation for extended explorations. Future research could focus on applying these findings to more complex flow scenarios, including turbulent flows or non-Newtonian fluids. Additionally, the potential application of these results in optimizing industrial processes, such as inkjet printing or drug delivery systems, represents an exciting avenue for practical implementation of our research.

By assuming a fully developed flow and under viscoelastic conditions the equations can be simplified as:

$$\tilde{\mathbf{u}} = [\dot{\gamma}_0 \tilde{y}, 0, 0]^\top, \quad (3.40)$$

where $\dot{\gamma}_0 = U_{\text{top}}/L$, represents the shear rate, with L being the distance between the plates.

In addition, we assume all partial derivatives with respect to x are equal to zero.

By applying the previously used scaling, the velocity can be further written as $\mathbf{u} = [y, 0, 0]^\top$, and consequently, the velocity gradient tensor is simplified to:

$$\nabla \mathbf{u} = \begin{pmatrix} 0 & 1 & 0 \\ 0 & 0 & 0 \\ 0 & 0 & 0 \end{pmatrix}. \quad (3.41)$$

All numerical computations were performed at the The University of South Carolina Hyperion High Performance Computing cluster, which is intended for large, parallel jobs and consists of 356 compute, GPU and Big Memory nodes, providing 16,616 CPU cores. Its compute and GPU nodes have 128-256 GB of RAM and Big Memory nodes have 2TB RAM. All nodes have EDR infiniband (100 Gb/s) interconnects, and access to 1.4 PB of GPFS storage. For our simulations we were using $N = 2^{18}$ GPU threads, each of which was in charge of one dumbbell.

In Figs. 3.3 and 3.4 we compare results of the Hookean single dumbbell model with parameters $dt_{\text{macro}} = 10^{-1}$, $dt_{\text{micro}} = 10^{-5}$ with the Upper Convected Maxwell model for

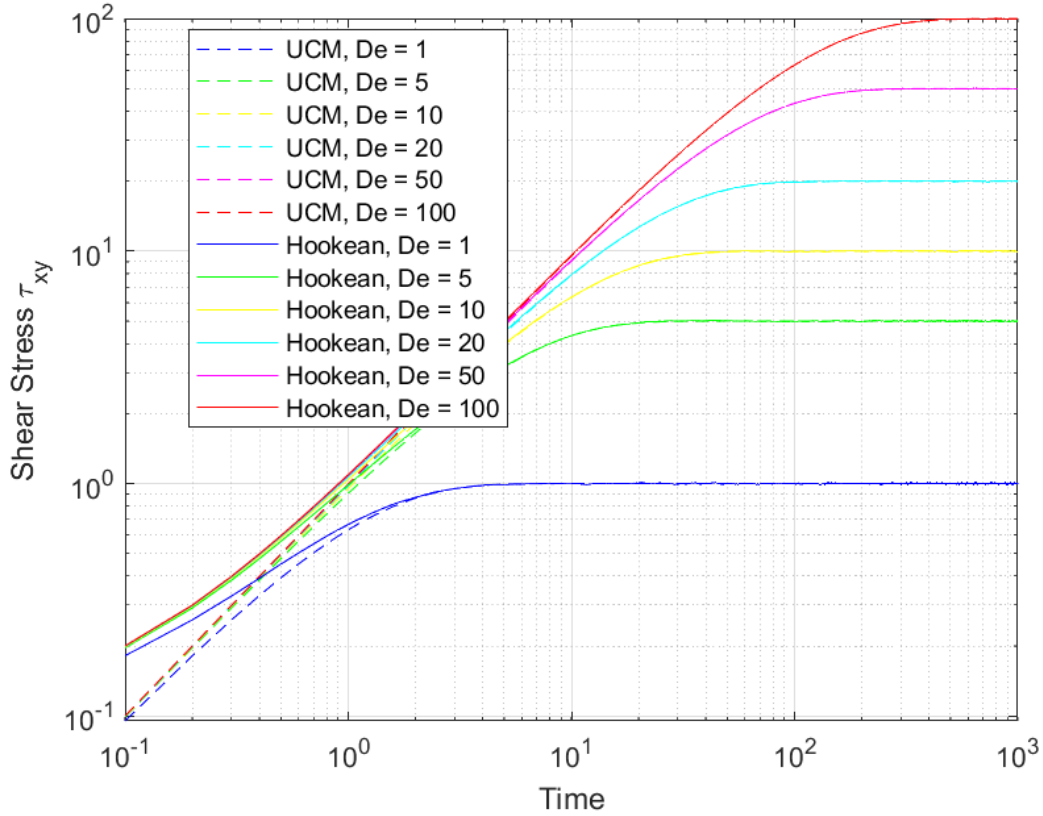


Figure 3.3 Comparison of shear stress results for Hookean model and its UCM closure, $dt_{\text{macro}} = 10^{-1}$, $dt_{\text{micro}} = 10^{-5}$.

varied values of the Deborah number De . In Fig. 3.3 we compare results of the shear stress component τ_{xy} , and in Fig. 3.4 we compare results of the first normal stress $N_1 = \tau_{xx} - \tau_{yy}$. The Upper Convected Maxwell model precisely follows the Hookean dumbbell equation, and as anticipated, outcomes from these two models consistently align.

Likewise, in Figs. 3.5 and 3.6 we compare results of the FENE single dumbbell model with parameters $dt_{\text{macro}} = 10^{-1}$, $dt_{\text{micro}} = 10^{-5}$, $b = 10^5$ with the FENE-P model for varied values of the Deborah number De . These figures illustrate that the FENE-P closure diverges from the FENE model as expected.

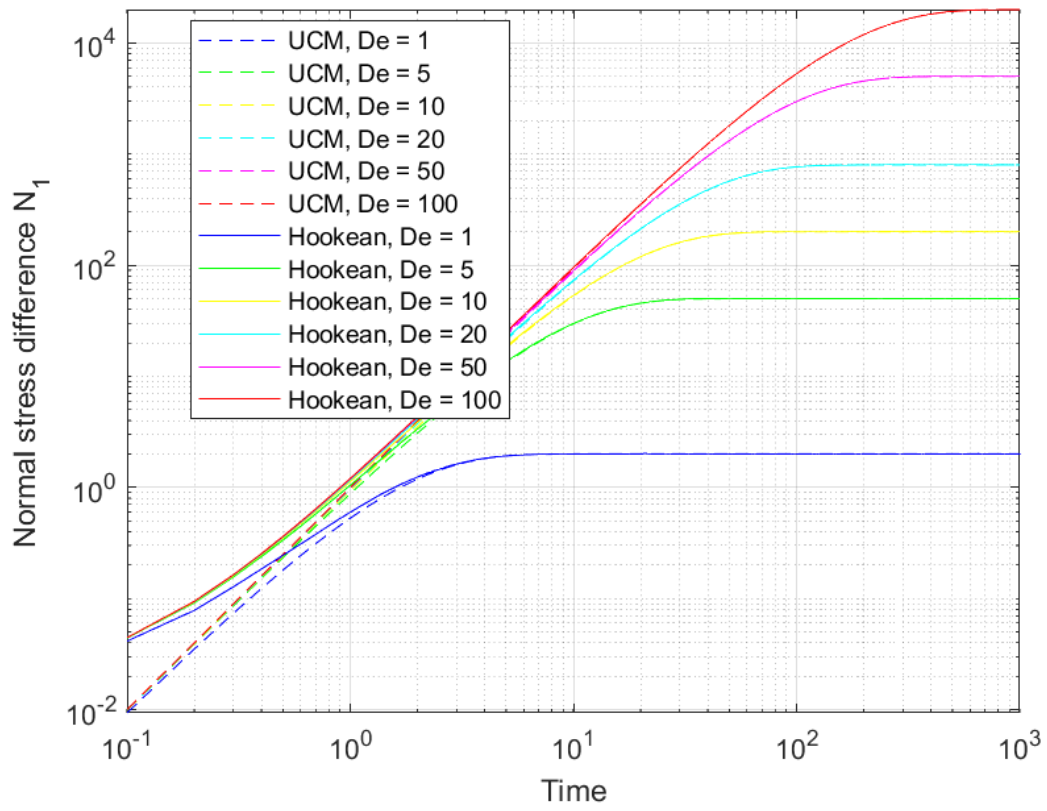


Figure 3.4 Comparison of normal stress $N_1 = \tau_{xx} - \tau_{yy}$ results for Hookean model and its UCM closure, $dt_{\text{macro}} = 10^{-1}$, $dt_{\text{micro}} = 10^{-5}$.

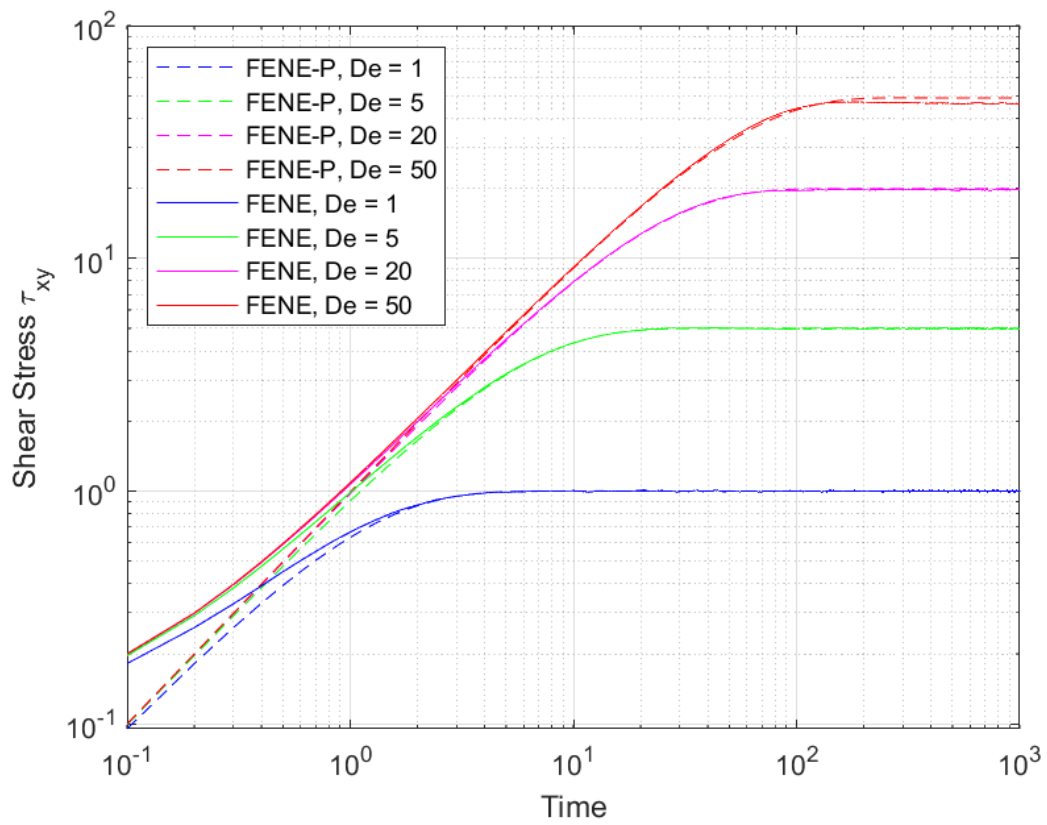


Figure 3.5 Comparison of shear stress results for FENE and FENE-P models, $dt_{\text{macro}} = 10^{-1}$, $dt_{\text{micro}} = 10^{-5}$, $b = 10^5$.

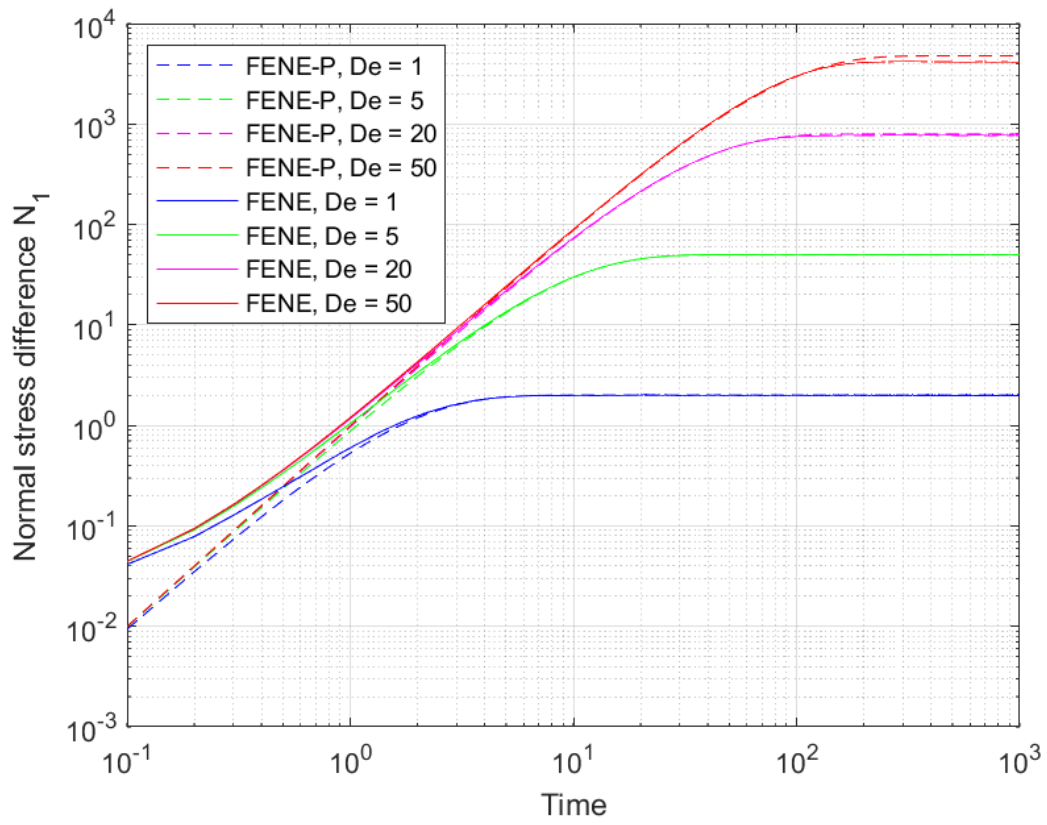


Figure 3.6 Comparison of normal stress N_1 results for FENE and FENE-P models, $dt_{\text{macro}} = 10^{-1}$, $dt_{\text{micro}} = 10^{-5}$, $b = 10^5$.

CHAPTER 4

MODELING STIMULI RESPONSIVE MATERIALS

4.1 CONSTITUTIVE MODELING

In order to incorporate the effects of external flow fields on the breaking and reforming dynamics of polymer chains, it becomes necessary to revise the dumbbell models described in Chapter 3. As a starting point, it is important to recognize that this new system comprises chains of various lengths. As an initial approximation, we simplify by assuming the existence of just two lengths. Therefore, there will be two types of dumbbells: single dumbbells and double dumbbells, which are formed by combining two single dumbbells. Besides the constitutive equations for the double dumbbells, we must also include processes that account for the combination of two single dumbbells to form a double dumbbell (reforming) and the separation of a double dumbbell into two single dumbbells (breaking). These approaches will be discussed in the following sections.

4.1.1 DOUBLE DUMBBELL REPRESENTATION

In a case of a double dumbbell we have two single dumbbells connected with a junction with the drag coefficient of 2ζ (Fig. 4.1). We begin with providing Langevin equation for the free beads $\mathbf{r}_1, \mathbf{r}_3$ and the junction bead \mathbf{r}_2 :

$$\frac{d\tilde{\mathbf{r}}_1}{dt} = (\tilde{\nabla}\tilde{\mathbf{u}})^T \cdot \tilde{\mathbf{r}}_1 - \frac{1}{\zeta}\mathbf{F}(\tilde{\mathbf{r}}_{1,2}) + \sqrt{\frac{2k_B T}{\zeta}}\mathbf{f}_1, \quad (4.1)$$

$$\frac{d\tilde{\mathbf{r}}_2}{dt} = (\tilde{\nabla}\tilde{\mathbf{u}})^T \cdot \tilde{\mathbf{r}}_2 - \frac{1}{2\zeta}(\mathbf{F}(\tilde{\mathbf{r}}_{2,1}) + \mathbf{F}(\tilde{\mathbf{r}}_{2,3})) + \sqrt{\frac{2k_B T}{2\zeta}}\mathbf{f}_2, \quad (4.2)$$

$$\frac{d\tilde{\mathbf{r}}_3}{dt} = (\tilde{\nabla}\tilde{\mathbf{u}})^T \cdot \tilde{\mathbf{r}}_3 - \frac{1}{\zeta}\mathbf{F}(\tilde{\mathbf{r}}_{3,2}) + \sqrt{\frac{2k_B T}{\zeta}}\mathbf{f}_3. \quad (4.3)$$

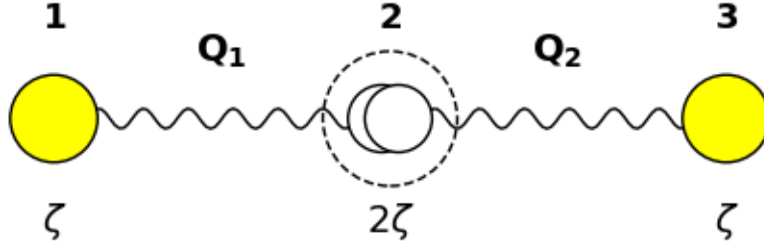


Figure 4.1 Double dumbbell configuration given by two free beads with a drag coefficient ζ and the junction with a drag coefficient 2ζ .

Rewriting these equations in terms of the end-to-end connector vectors gives:

$$\frac{d\mathbf{Q}_1}{dt} = (\nabla\mathbf{u})^T \cdot \mathbf{Q}_1 - \frac{1}{2\zeta}\mathbf{F}(\mathbf{r}_{2,1}) - \frac{1}{2\zeta}\mathbf{F}(\mathbf{r}_{2,3}) + \frac{1}{\zeta}\mathbf{F}(\mathbf{r}_{1,2}) + \sqrt{\frac{2k_B T}{\zeta}}\left(\frac{1}{\sqrt{2}}\mathbf{f}_2 - \mathbf{f}_1\right), \quad (4.4)$$

$$\frac{d\mathbf{Q}_2}{dt} = (\nabla\mathbf{u})^T \cdot \mathbf{Q}_2 - \frac{1}{\zeta}\mathbf{F}(\mathbf{r}_{3,2}) + \frac{1}{2\zeta}\mathbf{F}(\mathbf{r}_{2,1}) + \frac{1}{2\zeta}\mathbf{F}(\mathbf{r}_{3,2}) + \sqrt{\frac{2k_B T}{\zeta}}\left(\frac{1}{\sqrt{2}}\mathbf{f}_1 - \mathbf{f}_2\right), \quad (4.5)$$

which could be simplified to:

$$\frac{d\mathbf{Q}_1}{dt} = (\nabla\mathbf{u})^T \cdot \mathbf{Q}_1 - \frac{1}{2\zeta}(3\mathbf{F}(\mathbf{Q}_1) - \mathbf{F}(\mathbf{Q}_2)) + \sqrt{\frac{3k_B T}{\zeta}}d\mathbf{W}_t, \quad (4.6)$$

$$\frac{d\mathbf{Q}_2}{dt} = (\nabla\mathbf{u})^T \cdot \mathbf{Q}_2 - \frac{1}{2\zeta}(3\mathbf{F}(\mathbf{Q}_2) - \mathbf{F}(\mathbf{Q}_1)) + \sqrt{\frac{3k_B T}{\zeta}}d\mathbf{W}_t. \quad (4.7)$$

- *Equations for Double Hookean Dumbbells*

Applying Hookean force, we can rewrite Eqns. (4.6) and (4.7) as follows:

$$\frac{d\mathbf{Q}_1}{dt} = (\nabla\mathbf{u})^T \cdot \mathbf{Q}_1 - \frac{H}{2\zeta}(3\mathbf{Q}_1 - \mathbf{Q}_2) + \sqrt{\frac{3k_B T}{\zeta}}d\mathbf{W}_t, \quad (4.8)$$

$$\frac{d\mathbf{Q}_2}{dt} = (\nabla\mathbf{u})^T \cdot \mathbf{Q}_2 - \frac{H}{2\zeta}(3\mathbf{Q}_2 - \mathbf{Q}_1) + \sqrt{\frac{3k_B T}{\zeta}}d\mathbf{W}_t. \quad (4.9)$$

Using the same non-dimensional parameters as for the single dumbbell, we get non-

dimensional equations for a Hookean double dumbbell:

$$\frac{d\mathbf{Q}_1}{dt} = (\nabla\mathbf{u})^T \cdot \mathbf{Q}_1 - \frac{1}{8De}(3\mathbf{Q}_1 - \mathbf{Q}_2) + \sqrt{\frac{3}{4De}}d\mathbf{W}_t, \quad (4.10)$$

$$\frac{d\mathbf{Q}_2}{dt} = (\nabla\mathbf{u})^T \cdot \mathbf{Q}_2 - \frac{1}{8De}(3\mathbf{Q}_2 - \mathbf{Q}_1) + \sqrt{\frac{3}{4De}}d\mathbf{W}_t, \quad (4.11)$$

$$\boldsymbol{\tau} = \langle\langle \mathbf{Q}_1\mathbf{Q}_1 \rangle\rangle + \langle\langle \mathbf{Q}_2\mathbf{Q}_2 \rangle\rangle - \mathbf{I}. \quad (4.12)$$

- *Equations for Double FENE Dumbbells*

For a double dumbbell system under FENE forces, the equations corresponding to Eqns. (4.6) and (4.7) are modified using the same non-dimensionalization as in the single dumbbell case:

$$\frac{d\mathbf{Q}_1}{dt} = (\nabla\mathbf{u})^T \cdot \mathbf{Q}_1 - \frac{1}{8De} \frac{(3\mathbf{Q}_1 - \mathbf{Q}_2)}{1 - Q_1^2/b} + \sqrt{\frac{3}{4De}}d\mathbf{W}_t, \quad (4.13)$$

$$\frac{d\mathbf{Q}_2}{dt} = (\nabla\mathbf{u})^T \cdot \mathbf{Q}_2 - \frac{1}{8De} \frac{(3\mathbf{Q}_2 - \mathbf{Q}_1)}{1 - Q_2^2/b} + \sqrt{\frac{3}{4De}}d\mathbf{W}_t, \quad (4.14)$$

$$\boldsymbol{\tau} = \left\langle\left\langle \frac{\mathbf{Q}_1\mathbf{Q}_1}{1 - Q_1^2/b} \right\rangle\right\rangle + \left\langle\left\langle \frac{\mathbf{Q}_2\mathbf{Q}_2}{1 - Q_2^2/b} \right\rangle\right\rangle - \mathbf{I}. \quad (4.15)$$

4.1.2 BREAKING DYNAMICS

In this work we are using the detachment mechanism, based on the model proposed by Hernandez Cifre et al. [28]. which involves a consideration of the energy barriers and the lifetime of junctions formed by beads in the network. The lifetime of a junction τ in the network is modeled as a function of the energy barrier that must be overcome for bead detachment:

$$\tau = \tau_0 e^{\frac{-d_0^2 F_s^2}{4U_0}}, \quad (4.16)$$

where τ_0 is the mean life time of a junction without stretch, F_s is the elastic force acting on the bead due to the connector spring, U_0 and d_0 are depth and width of the parabolic potential well. This leads to having following probability of detachment per time step:

$$P_{\text{dissoc}} = 1 - \exp\left(-\frac{\Delta t}{\tau}\right). \quad (4.17)$$

4.1.3 REFORMING DYNAMICS

In our model, since we are not monitoring the specific locations of each dumbbell, it is not feasible to determine if two dumbbells are within a range where they could potentially connect. To address this, we introduce a mean reforming rate, denoted as $1/\beta_0$ [19]. This rate is designed to approximate the effect of the density of dumbbells in the system. Essentially, it represents an average rate at which separated dumbbells could come together to form a bond, reflecting the overall likelihood of reattachment in the absence of precise positional information. This approach leads to having following probability of attachment per time step:

$$P_{\text{assoc}} = 1 - \exp\left(-\frac{\Delta t}{\beta_0}\right). \quad (4.18)$$

4.2 NUMERICAL SCHEMES

In our approach, when a single dumbbell has to be changed to a double dumbbell, we manually attach a second single dumbbell with the same \mathbf{Q} value, and when a double dumbbell breaks into two single dumbbells we keep tracking one of them and pretend that the second one does not exist anymore. A significant contribution of this research is the development of a novel approach for transitioning single dumbbells to double dumbbells within our simulations. This method manages to mirror the physical processes of bead attachment and detachment in polymer networks while maintaining computational efficiency under GPU restrictions of this numerical scheme.

4.2.1 INITIALIZATION STEPS

In the initial stages of the simulation, the system parameters and variables undergo initialization. This involves configuring various elements such as the number of threads (referred to as dumbbells), the Deborah number De , the maximum spring extension b , the deformation tensor κ , as well as parameters τ_0 and β_0 associated with detachment and attachment probabilities. Additionally, three distinct time steps (dt_{macro} , dt_{prob} , dt_{micro}) are established.

4.2.2 CALCULATION OF ATTACHMENT AND DETACHMENT PROBABILITIES

ATTACHMENT

For a single dumbbell ($Q_{\text{type}} = 1$) at each dt_{prob} time step we calculate the probability of attachment:

$$p_{\text{attach}} = 1 - \exp\left(-\frac{dt_{\text{prob}}}{\beta_0}\right). \quad (4.19)$$

Using Monte-Carlo approach, we compare calculated probability of attachment with a generated uniformly distributed random number. If p_{attach} is greater, the dumbbell changes to a double dumbbell. In our modeling approach, we achieve this by assigning the \mathbf{Q} value from the first dumbbell to the second. This method enables our model to maintain average orientations and stretching of the dumbbells within the constraints of non-interacting GPU threads.

DETACHMENT

For a double dumbbell ($Q_{\text{type}} = 2$) at each dt_{prob} time step we calculate the probability of detachment:

$$p_{\text{detach}} = 1 - \exp\left(-\frac{dt_{\text{prob}}}{\tau}\right), \quad (4.20)$$

$$\tau = \tau_0 \exp\left(-\frac{d_0^2}{4U_0} \left(\frac{Q_a}{Q_{mx}}\right)^2\right), \quad (4.21)$$

where Q_a is the maximum magnitude of the two dumbbells, and $Q_{mx} = 1 - \left(\frac{Q_a}{Q_{\max}}\right)^2$. For our simulations, we assume $\frac{d_0^2}{4U_0} \approx 0.004$ based on the values used in [28], so the probability of detachment can be varied by changing the values of only one parameter τ_0 :

$$p_{\text{detach}} = 1 - \exp\left(-\frac{dt_{\text{prob}}}{\tau}\right), \quad (4.22)$$

$$\tau = \tau_0 \exp\left(-0.004 \left(\frac{Q_a}{Q_{mx}}\right)^2\right). \quad (4.23)$$

Here probability of detachment directly relates to the maximum of extensions of the springs. Similar to the attachment case, a generated uniformly distributed random number is compared to probability of detachment. If p_{detach} is greater, the dumbbell detaches into a single dumbbell.

4.2.3 HOOKEAN DUMBBELLS EVOLUTION

In the case of Hookean Dumbbells, we are using a forward Euler scheme. For each double dumbbell we are solving Eqns. (4.10) and (4.11) and we get the following scheme:

$$\begin{aligned} \mathbf{Q}_1(t_{j+1}) = & \left[(\nabla \mathbf{u})^T \cdot \mathbf{Q}_1(t_j) - \frac{1}{8De} (3\mathbf{Q}_1(t_j) - \mathbf{Q}_2(t_j)) \right] \Delta t_j \\ & + \mathbf{Q}_1(t_j) + \sqrt{\frac{3}{4De}} \Delta \mathbf{W}_{1,j}, \end{aligned} \quad (4.24)$$

$$\begin{aligned} \mathbf{Q}_2(t_{j+1}) = & \left[(\nabla \mathbf{u})^T \cdot \mathbf{Q}_2(t_j) - \frac{1}{8De} (3\mathbf{Q}_2(t_j) - \mathbf{Q}_1(t_j)) \right] \Delta t_j \\ & + \mathbf{Q}_2(t_j) + \sqrt{\frac{3}{4De}} \Delta \mathbf{W}_{2,j}. \end{aligned} \quad (4.25)$$

4.2.4 FENE DUMBBELLS EVOLUTION

In the case of FENE Dumbbells due to the introduction of non-linearity in the evolution equation, a semi-implicit algorithm of the first order is employed instead of the forward Euler scheme.

PREDICTOR STEP

The predictor step computes intermediate connector vectors \mathbf{S}_1 and \mathbf{S}_2 for each dumbbell [27, 30]:

$$\mathbf{S}_1 = \mathbf{Q}_1(t_j) + \left[(\nabla \mathbf{u})^T \cdot \mathbf{Q}_1(t_j) - \frac{F_1(\mathbf{Q}(t_j))}{2De} \right] \Delta t_j + \sqrt{\frac{3}{4De}} \Delta \mathbf{W}_{1,j} \quad (4.26)$$

$$\mathbf{S}_2 = \mathbf{Q}_2(t_j) + \left[(\nabla \mathbf{u})^T \cdot \mathbf{Q}_2(t_j) - \frac{F_2(\mathbf{Q}(t_j))}{2De} \right] \Delta t_j + \sqrt{\frac{3}{4De}} \Delta \mathbf{W}_{2,j}, \quad (4.27)$$

where $\mathbf{Q}_1(t_j)$ and $\mathbf{Q}_2(t_j)$ are the current end-to-end connector vector, $F_1(\mathbf{Q}(t_j))$ and $F_2(\mathbf{Q}(t_j))$ are related to the FENE spring force and we define them as:

$$F_1(\mathbf{Q}(t_j)) = \frac{1}{4} \left(\frac{3\mathbf{Q}_1(t_j)}{1 - \mathbf{Q}_1(t_j)^2/b} - \frac{\mathbf{Q}_2(t_j)}{1 - \mathbf{Q}_2(t_j)^2/b} \right), \quad (4.28)$$

$$F_2(\mathbf{Q}(t_j)) = \frac{1}{4} \left(\frac{3\mathbf{Q}_2(t_j)}{1 - \mathbf{Q}_2(t_j)^2/b} - \frac{\mathbf{Q}_1(t_j)}{1 - \mathbf{Q}_1(t_j)^2/b} \right), \quad (4.29)$$

which we can rewrite as:

$$F_1(\mathbf{Q}(t_j)) = \frac{3F(\mathbf{Q}_1(t_j)) - F(\mathbf{Q}_2(t_j))}{4}, \quad (4.30)$$

$$F_2(\mathbf{Q}(t_j)) = \frac{3F(\mathbf{Q}_2(t_j)) - F(\mathbf{Q}_1(t_j))}{4}, \quad (4.31)$$

CORRECTOR STEP

The corrector step refines connector vectors based on the predictor step:

$$\begin{aligned} \mathbf{Q}_1(t_{j+1}) \left[1 + \frac{3}{16De} \frac{\Delta t_j}{1 - \mathbf{Q}_1^2(t_{j+1})/b} \right] &= \mathbf{Q}_1(t_j) + \sqrt{\frac{1}{De}} \Delta \mathbf{W}_{1,j} \\ &+ \frac{\Delta t_j}{2} \left[(\nabla \mathbf{u})^T \cdot \mathbf{S}_1 + (\nabla \mathbf{u})^T \cdot \mathbf{Q}_1(t_j) \right] \\ &+ \frac{\Delta t_j}{16De} [F(\mathbf{Q}_2(t_j)) - 3F(\mathbf{Q}_1(t_j))], \end{aligned} \quad (4.32)$$

$$\begin{aligned}
\mathbf{Q}_2(t_{j+1}) \left[1 + \frac{3}{16De} \frac{\Delta t_j}{1 - Q_2^2(t_{j+1})/b} \right] &= \mathbf{Q}_2(t_j) + \sqrt{\frac{1}{De}} \Delta \mathbf{W}_{2,j} \\
&+ \frac{\Delta t_j}{2} [(\nabla \mathbf{u})^T \cdot \mathbf{S}_2 + (\nabla \mathbf{u})^T \cdot \mathbf{Q}_2(t_j)] \\
&+ \frac{\Delta t_j}{16De} [F(\mathbf{Q}_1(t_j)) - 3F(\mathbf{Q}_2(t_j))].
\end{aligned} \tag{4.33}$$

CUBIC EQUATION

To get [new end-to-end connector vectors](#) from the previous corrector step, we need to solve the following cubic equations, which have unique real solutions in $(0, \sqrt{b})$ [31]:

$$x_1^3 - P_1 x_1^2 - b \left(1 + \frac{3}{16De} \Delta t_j \right) x_1 + b P_1 = 0 \tag{4.34}$$

$$x_2^3 - P_2 x_2^2 - b \left(1 + \frac{3}{16De} \Delta t_j \right) x_2 + b P_2 = 0, \tag{4.35}$$

where \mathbf{P}_1 and \mathbf{P}_2 are the the right-hand-sides of the previous corrector step Eqns. (4.32) and (4.32). P_1 and P_2 are the magnitudes of \mathbf{P}_1 and \mathbf{P}_2 respectively.

POSITION UPDATE

The new end-to-end connector vectors of each dumbbell are updated according to the following formulas:

$$\mathbf{Q}_1(t_{j+1}) = x_1 \cdot \frac{\mathbf{P}_1}{P_1} \tag{4.36}$$

$$\mathbf{Q}_2(t_{j+1}) = x_2 \cdot \frac{\mathbf{P}_2}{P_2}. \tag{4.37}$$

4.3 RESULTS

Similarly to Section 3.5 we present our results for a case of a simple shear flow, which is created by positioning a fluid between two parallel plates, where the bottom plate remains fixed and the top plate moves at a constant speed, denoted by U_{top} . By assuming a fully developed flow and under viscoelastic conditions the equations can be simplified as:

$$\tilde{\mathbf{u}} = [\dot{\gamma}_0 \tilde{y}, 0, 0]^\top, \quad (4.38)$$

where $\dot{\gamma}_0 = U_{\text{top}}/L$, represents the shear rate, with L being the distance between the plates. In addition, we assume all partial derivatives with respect to x are equal to zero.

By applying the previously used scaling, the velocity can be further written as $\mathbf{u} = [y, 0, 0]^\top$, and consequently, the velocity gradient tensor is simplified to:

$$\nabla \mathbf{u} = \begin{pmatrix} 0 & 1 & 0 \\ 0 & 0 & 0 \\ 0 & 0 & 0 \end{pmatrix}. \quad (4.39)$$

All numerical computations were performed at the The University of South Carolina Hyperion High Performance Computing cluster, which is intended for large, parallel jobs and consists of 356 compute, GPU and Big Memory nodes, providing 16,616 CPU cores. Its compute and GPU nodes have 128-256 GB of RAM and Big Memory nodes have 2TB RAM. All nodes have EDR infiniband (100 Gb/s) interconnects, and access to 1.4 PB of GPFS storage. For our simulations we were using $N = 2^{18}$ GPU threads, each of which was in charge of one dumbbell (either single or a double one).

In Figs. 4.2-4.5, we present results for a Hookean stochastic model with parameters $\tau_0 = 1$, $U_0 = 15$, $d_0 = 0.5$, $dt_{\text{macro}} = 1$, $dt_{\text{prob}} = 10^{-2}$, $dt_{\text{micro}} = 10^{-4}$, $b = 100$. We examine various values of the parameter β , which is related to the reforming rate of single dumbbells, and also consider different values of the Deborah number De . We initialize the system by setting all dumbbells to be single, with their \mathbf{Q} values drawn from the normal distribution with a mean of 0 and a variance of 1. In Fig. 4.2 we demonstrate how the number of single dumbbells changes in the system for $\beta = 0.001$ and $\beta = 0.01$. It can be seen that a lower

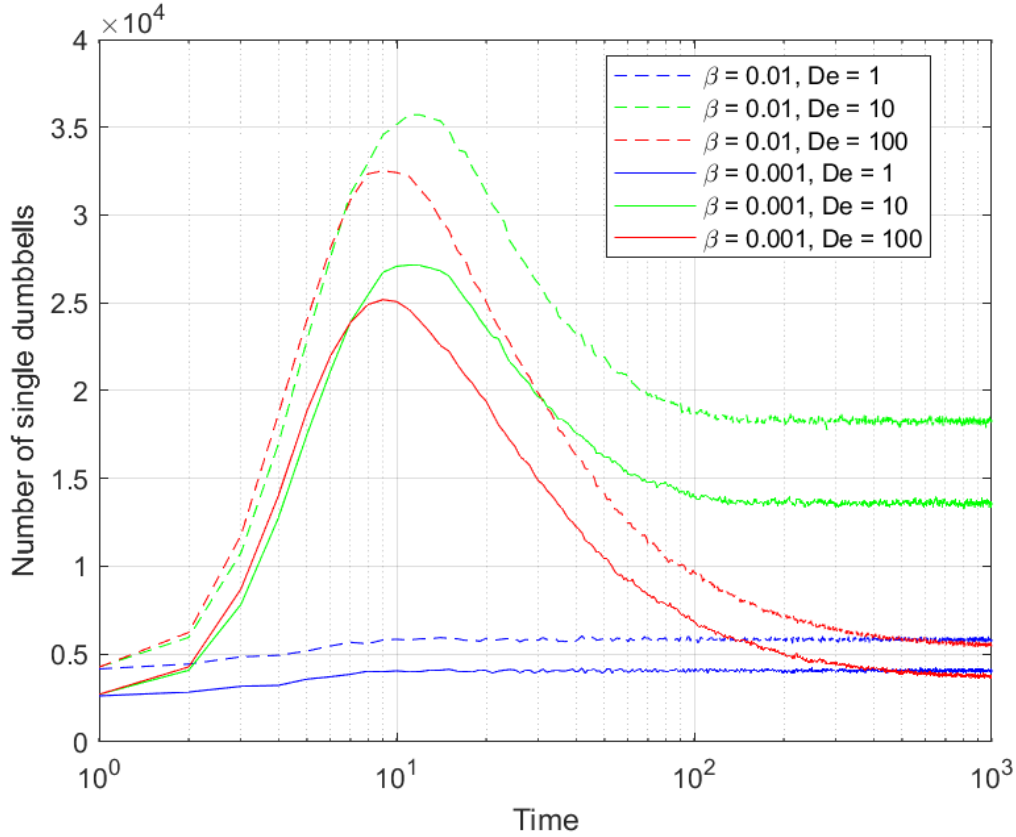


Figure 4.2 Comparison of number of single dumbbells for Hookean models with reforming rate $\beta = 0.01$ and $\beta = 0.001$.

value of β consistently results in a smaller number of single dumbbells, indicating that the system contains a larger number of double dumbbells, which have reformed from the single ones. This result aligns with our expectations, as the mean reforming rate, employed in our calculations of attachment probability in Eqn. (4.18), is inversely proportional to the β_0 value. In Figs. 4.3-4.4 we compare results for stress component τ_{xy} and first normal stress N_1 . As can be seen from the figures, different reforming rates yield similar results. In Fig. 4.5 we present results of the second normal stress, which we calculate as $N_2 = \tau_{yy} - \tau_{zz}$. The figure indicates that larger values of β tend to result in higher amplitudes. It can also be observed that the values of N_2 begin to stabilize concurrently with the stabilization of τ_{xy} and N_1 , as shown in Figs. 4.3-4.4.

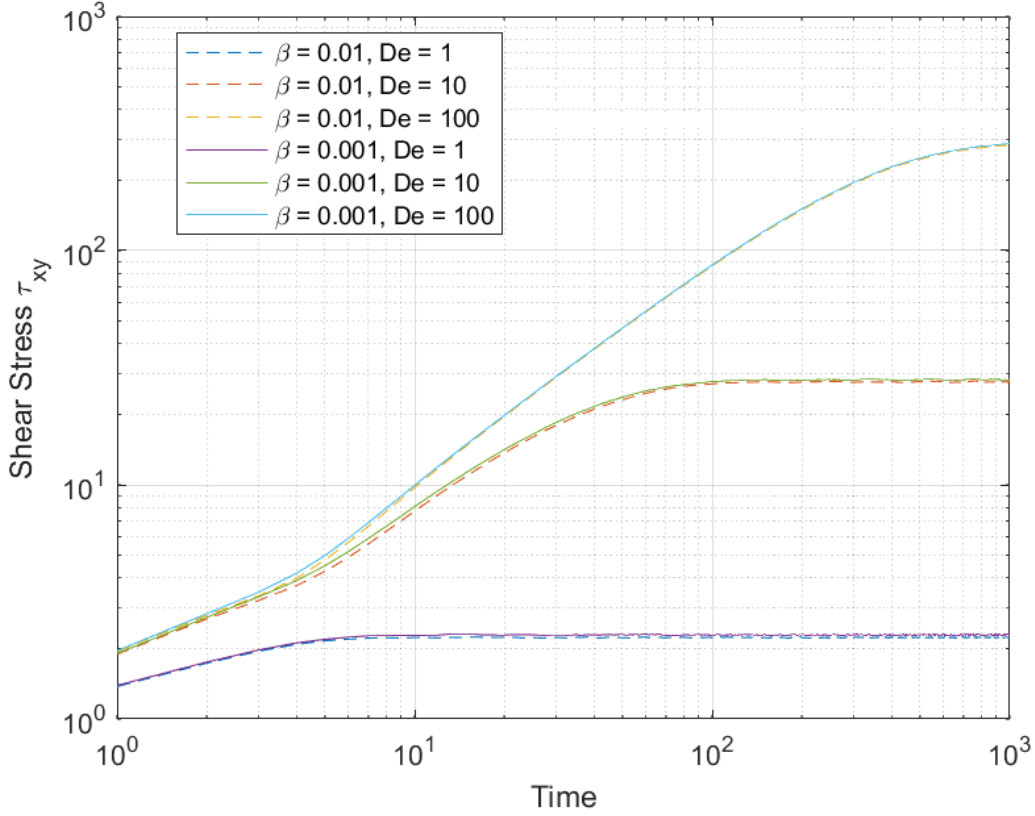


Figure 4.3 Comparison of shear stress for Hookean models with reforming rate $\beta = 0.01$ and $\beta = 0.001$.

In Figs. 4.6-4.9, we present results for a FENE stochastic model with parameters $\beta = 0.01$, $U_0 = 15$, $d_0 = 0.5$, $dt_{\text{macro}} = 1$, $dt_{\text{prob}} = 10^{-2}$, $dt_{\text{micro}} = 10^{-4}$, $b = 100$. We examine various values of the parameter τ_0 , which is related to the mean life time of a junction, and also consider different values of the Deborah number De . In Fig. 4.6 we demonstrate the variation in the number of single dumbbells within the system for $\tau_0 = 1$ and $\tau_0 = 16$. It is observed that a smaller value of τ_0 consistently leads to a higher number of single dumbbells, which have resulted from the reformation of double ones. This outcome is in line with our expectations, as the mean lifetime of a junction, used in our calculations of detachment probability in Eqn. (4.17), is inversely proportional to the τ_0 value. In Figs. 4.7-4.8 we compare results for stress component τ_{xy} and first normal stress N_1 . The figures

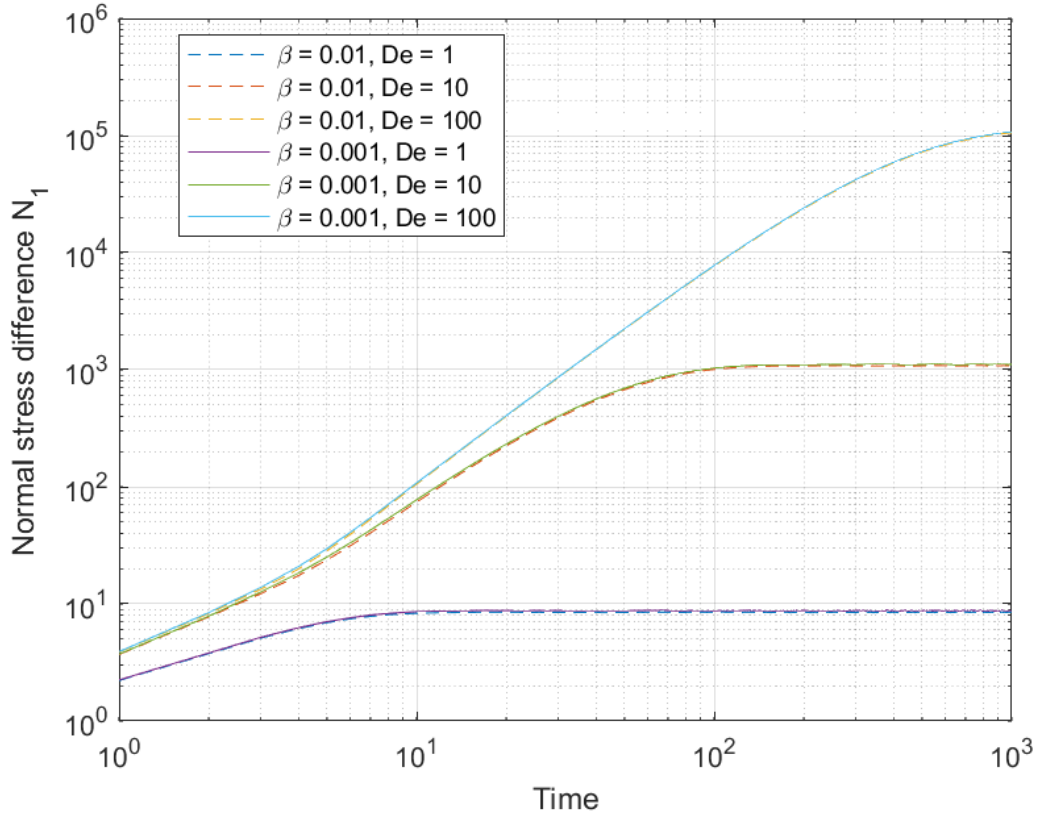


Figure 4.4 Comparison of normal stress N_1 results for Hookean models with reforming rate $\beta = 0.01$ and $\beta = 0.001$.

demonstrate that as the value of De increases, the results for different τ_{u_0} values converge. Additionally, it is noticeable how the profiles of the shear stress and first normal stress differ from those presented in Figs. 3.5-3.6, respectively. The primary reason for the significant bump observed before stabilization in Figs. 4.7-4.8 is attributed to using a smaller value of b , which represents the square of the maximum possible extension of the spring. In Fig. 4.9 we present results of the second normal stress. It is observed that larger values of De lead to higher amplitudes of N_2 . Moreover, Figs. 4.7-4.8 show that the stabilization of N_2 values occurs simultaneously with the stabilization of τ_{xy} and N_1 .

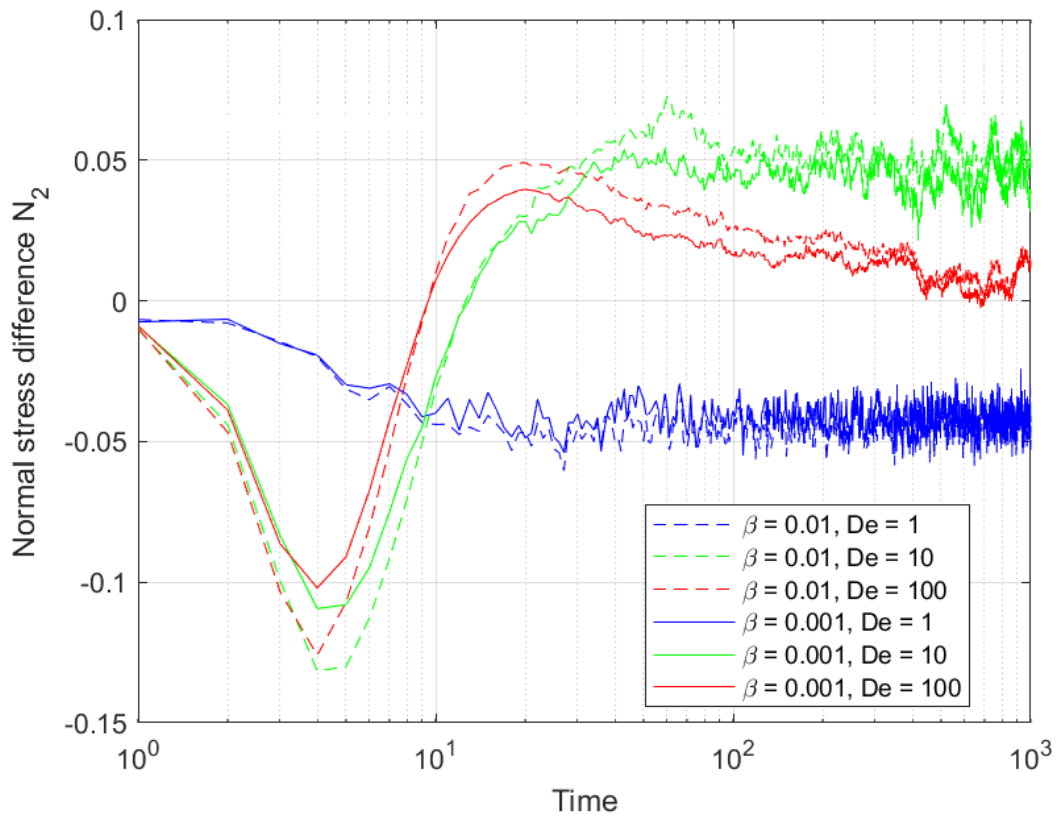


Figure 4.5 Comparison of normal stress N_2 results for Hookean models with reforming rate $\beta = 0.01$ and $\beta = 0.001$.

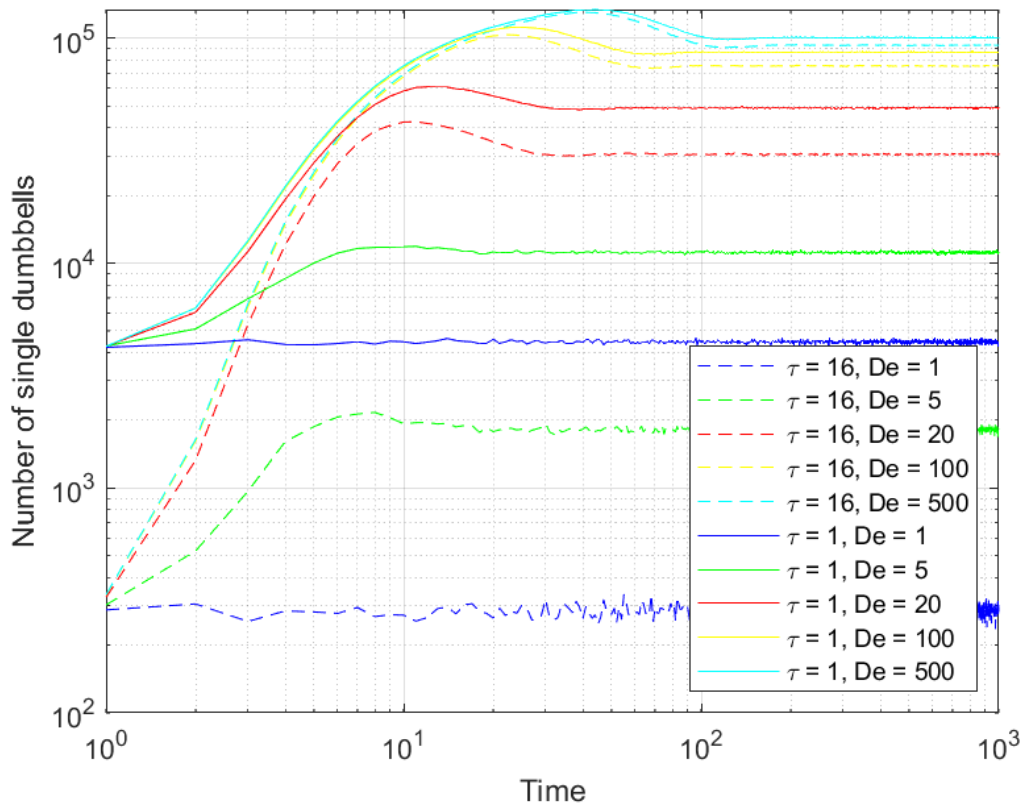


Figure 4.6 Comparison of number of single dumbbells for FENE models with breaking rate $\tau_0 = 16$ and $\tau_0 = 1$.

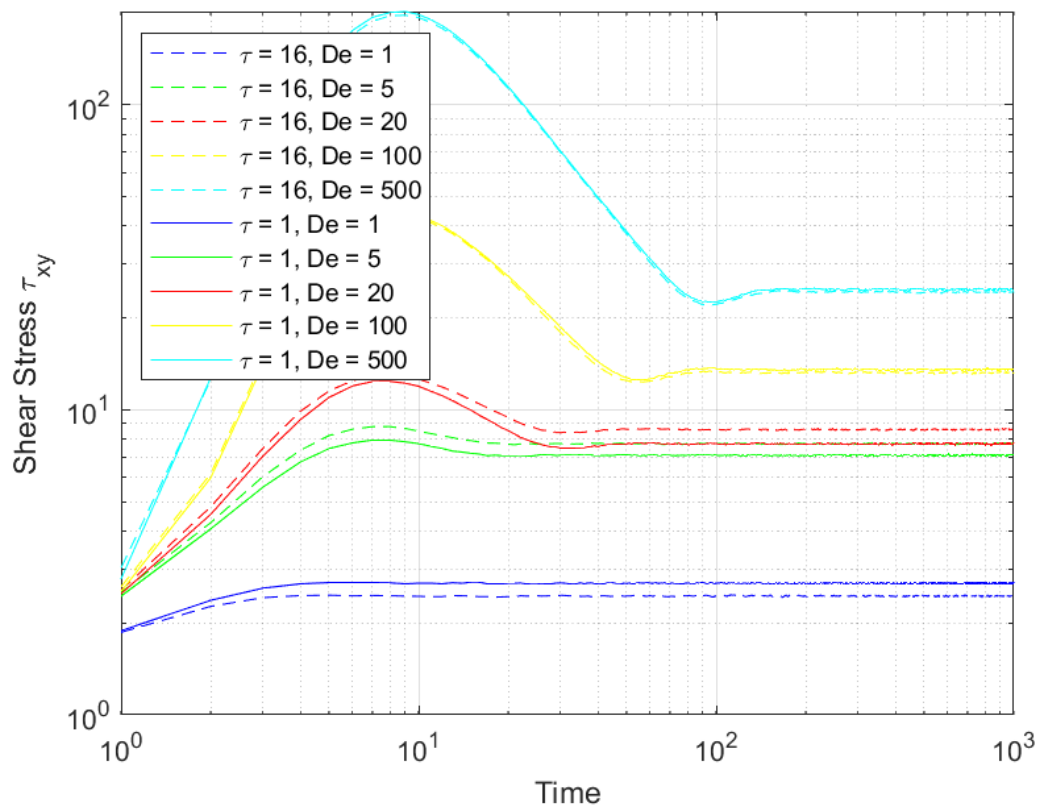


Figure 4.7 Comparison of shear stress for FENE models with breaking rate $\tau = 16$ and $\tau = 1$.

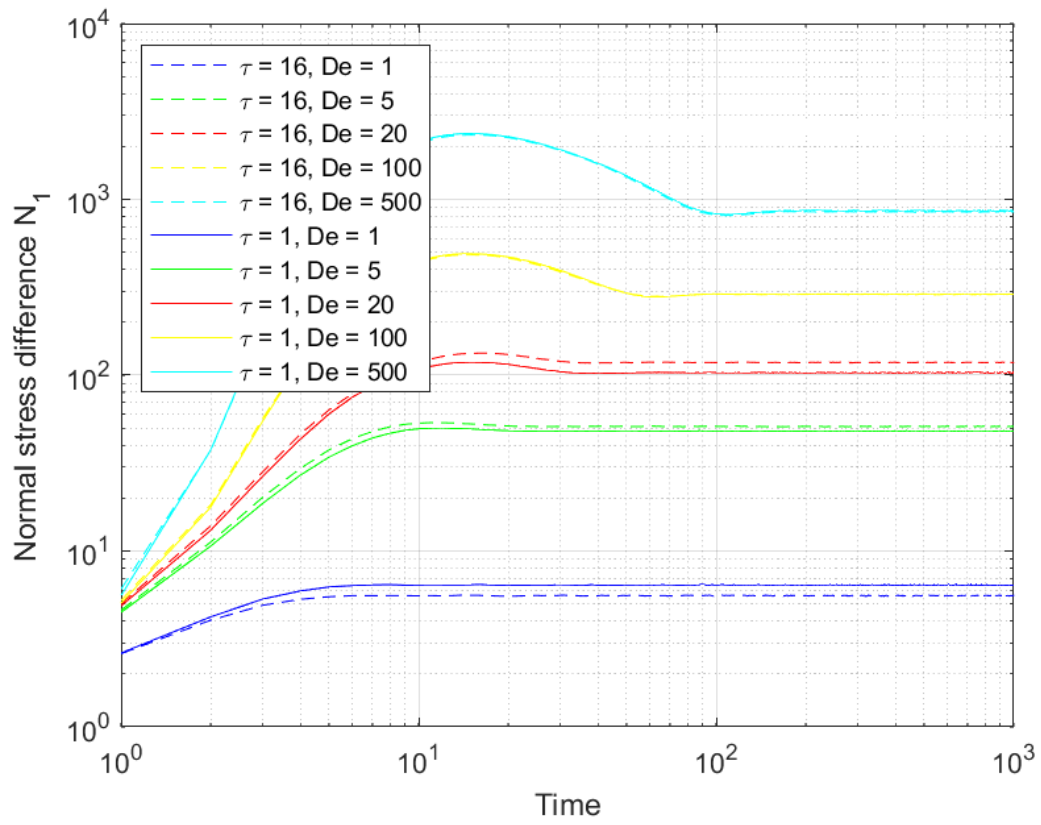


Figure 4.8 Comparison of normal stress N_1 results for FENE models with breaking rate $\tau = 16$ and $\tau = 1$.

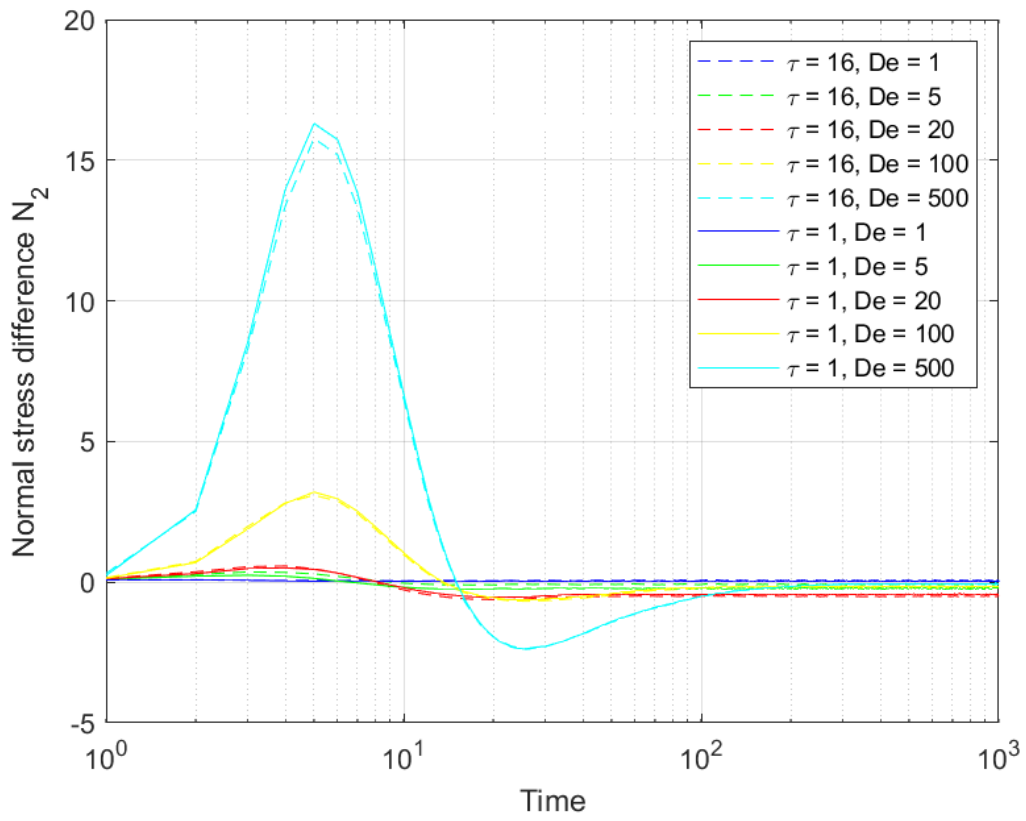


Figure 4.9 Comparison of normal stress N_2 results for FENE models with breaking rate $\tau = 16$ and $\tau = 1$.

CHAPTER 5

DISCUSSION

5.1 CONCLUDING REMARKS

This dissertation combines mathematical modeling and simulation to examine the behavior of viscoelastic materials. Our primary concern is the description of polymer networks at the mesoscale, with a connection to the macroscopic conservation equations.

In Chapter 2, we explore the connection between Langevin (LE) and Fokker-Planck (FP) representations of particles diffusing in a fluid, both with and without external fields. While each description offers a different perspective on the underlying dynamics, there is a direct connection between these two approaches. To explore this connection, we provide simple examples of both one and two dimensions. In studying these two families of equations, we employ subjects from calculus, such as Taylor expansions and conservative vector fields; as well as ordinary differential equations, such as integrating factors; and partial differential equations, such as similarity solutions.

The LE representation involves stochastic differential equations (SDEs) and allows for the easy incorporation of microscopic processes into the equations. However, a drawback of this representation is that it requires as many SDEs as degrees of freedom in the system, and each SDE needs to be solved multiple times to reduce statistical noise. The FP approach involves partial differential equations (PDEs) that describe the evolution of the probability density function (PDF) of the stochastic variable. Unlike numerical solutions for SDEs, solutions for the FP equations are deterministic. However, a drawback of the FP approach is that the dimensionality of the PDF increases with the number of degrees of freedom in the system, leading to high algorithmic complexity and a high computational cost for the corresponding numerical schemes.

Experimentally, LE equations can be informed by techniques that capture the movement of probes at the microscale, such as passive microrheology [40]. While, FP equations can be informed by experimental techniques that capture the behavior of the ensemble of probes, such as light scattering experiments [46].

In Chapter 3, we study constitutive modeling of polymeric solutions. To facilitate highly parallel and efficient simulations, we present a multiscale flow solver that harnesses the power of GPU computing. The core element of this work is the dumbbell model, which allows us to investigate the behavior of polymer chains in complex fluids. In our study, we explore two types of spring laws: the linear spring law, which gives rise to the Hookean model, and the nonlinear law, which leads to the FENE model. To ensure the accuracy and reliability of our approach, we rigorously validate it against macroscopic constitutive equations. The results of this validation confirm the effectiveness of our simulation techniques in accurately capturing the intricate behavior of polymer chains.

Through the improvement of computational capabilities, our work makes it possible to simulate large-scale systems that were previously unattainable due to computational constraints. This development has significant implications in various industries, such as materials science, biotechnology, and pharmaceuticals. Moreover, it improves the efficiency and advancement of technologies, such as 3D printing and drug delivery systems.

After validating this model through simulations of single dumbbells, we introduce a new modeling approach in Chapter 4. This approach involves incorporating breaking and reforming dynamics into the equations. The inclusion of these dynamics is crucial, as it enables the accurate simulation of systems where polymer chains undergo scission and recombination under the influence of external fields. This has direct applications in the field of stimuli-responsive materials. Stimuli-responsive materials are materials that can change their properties in response to external fields such as light, heat, electricity or flow. This ability to adapt makes them incredibly important for developing new technologies in medicine, energy, oil recovery and consumer products.

In our case, we use our simulations to study the behavior of reversible polymer networks under shear. Our approach allows us to capture the principal features of reversible polymer

networks, including a Newtonian plateau, which is a region of constant viscosity observed at low shear rates and shear thinning, which is the decrease in viscosity at high shear rates. Overall, this approach provides a computationally efficient way to model the behavior of these systems under shear.

5.2 FUTURE WORK

We aim to further refine the micro-macro approach for modeling complex micropolymer solutions, incorporating the Navier-Stokes equations. One of the next steps in our research is the development of a model adept at handling more complex geometries of polymeric chains and exploring the dynamic breaking and reforming processes. Investigating these structures could uncover new insights into the behavior of polymers under extreme conditions, paving the way for advanced materials with tailor-made properties for specific industrial applications. This will involve refining the current modeling approach to accurately represent and predict the behavior of polymers with intricate structural configurations. This development will entail creating advanced constitutive models that more precisely depict the intricate behaviors of polymer chains, such as entanglement, alignment, and stretching under diverse flow conditions. This particularly focuses on scenarios like elongational flow or capillary thinning, which were not covered in this work. Such advancements are crucial for a better understanding of the dynamics of these complex systems and for accurately simulating their behavior in diverse applications. Additionally, we plan to further investigate the implementation of efficient and accurate numerical methods for solving this complex system of coupled equations, with a special emphasis on leveraging GPU computations to enhance computational performance.

BIBLIOGRAPHY

- [1] Reith, D.; Mirny, L.; Virnau, P. GPU Based Molecular Dynamics Simulations of Polymer Rings in Concentrated Solution: Structure and Scaling. *Progress of Theoretical Physics Supplement* **2011**, *191*, 135–145. <https://doi.org/10.1143/PTPS.191.135>.
- [2] Brito, C.; Almeida, M.; e Silva, A.; Teixeira, J.; Teichrieb, V. Large viscoelastic fluid simulation on GPU,”. *XVI Simpósio Brasileiro de Jogos e Entretenimento Digital (SBGames)* **2017**, pp. 462–469.
- [3] Ingelsten, S.; Mark, A.; Jareteg, K.; Kádár, R.; Edelvik, F. Computationally Efficient Viscoelastic Flow Simulation Using a Lagrangian-Eulerian Method and GPU-acceleration. *Journal of Non-Newtonian Fluid Mechanics* **2020**, *279*, 104264. <https://doi.org/10.1016/j.jnnfm.2020.104264>
- [4] Yang, K.; Su, J.; Guo, H. GPU accelerated numerical simulations of viscoelastic phase separation model. *Journal of Computational Chemistry* **2012**, *33*, 1564–1571.
- [5] Bergamasco, L.; Izquierdo, S.; Ammar, A. Direct numerical simulation of complex viscoelastic flows via fast lattice-Boltzmann solution of the Fokker–Planck equation. *Journal of Non-Newtonian Fluid Mechanics* **2013**, *201*, 29–38.
- [6] Le Bris, C.; Lelièvre, T. Multiscale modelling of complex fluids: a mathematical initiation. In *Multiscale modeling and simulation in science* Lect. Notes Comput. Sci. Eng. **66**, Springer, Berlin (2009).
- [7] Keunings, R. Micro-Macro Methods for the Multiscale Simulation of Viscoelastic Flow Using Molecular Models of Kinetic Theory. *Rheology Reviews* **2004**, pp. 67–98.
- [8] Bird, R.B.; Curtiss, C.F.; Armstrong, R.C.; Hassager, O. *Dynamics of Polymeric Liquids, Volume 2: Kinetic Theory*; Wiley, 1987.
- [9] Yamamoto, M., The visco-elastic properties of network structure I. General formalism, *J. Phys. Soc. Japan* **11** (1956) 413–421.

- [10] Tanaka, F., Edwards, S.F. , Viscoelastic properties of physically cross-linked networks: 1. transient network theory, *Macromolecules* 25 (1992) 1516–1523.
- [11] Green, M.S., Tobolsky, A.V., A new approach to the theory of relaxing polymeric media, *J. Chem. Phys.* 14 (1946) 80–92.
- [12] B. van den Brule, P. Hoogerbrugge, Brownian dynamics simulation of reversible polymeric networks, *J. Non-Newton. Fluid Mech.* 60 (1995) 303–334.
- [13] McKinley, G. & Sridhar, T. Filament-stretching rheometry of complex fluids. *Annual Review Of Fluid Mechanics.* **34**, 375-415 (2002)
- [14] A. Vaccaro, G. Marrucci, A model for the nonlinear rheology of associating polymers, *J. Non-Newton. Fluid Mech.* 92 (2000) 261–273.
- [15] E. Rincón, A.E. Chávez, R. Herrera, O. Manero, Rheological modelling of complex fluids: A transient network model with microstates, *J. Non-Newton. Fluid Mech.* 131 (2005) 67–77.
- [16] Vasquez, P. A., McKinley, G. H., Cook L.P., A network scission model for worm-like micellar solutions. I. Model formulation and viscometric flow predictions, *J. Non-Newton. Fluid Mech.* 144, 122–139 (2007).
- [17] A.A. Adams, M.J. Solomon, R.G. Larson, A nonlinear kinetic-rheology model for reversible scission and deformation of unentangled wormlike micelles, *J. Rheol.* 62 (6) (2018) 1419–1427.
- [18] G.W. Park, G. Ianniruberto, A new stochastic simulation for the rheology of telechelic associating polymers, *J. Rheol.* 61 (2017) 1293–1305.
- [19] Quintero, L.E.F., Zhou, L., Cook, L.P., Transiently linked nonlinear FENE two species dynamics, *Journal of Non-Newtonian Fluid Mechanics*, Volume 301, 2022, 104720, ISSN 0377-0257,
- [20] Cromer, M.; Vasquez, P.A. Macro–Micro–Coupled Simulations of Dilute Viscoelastic Fluids. *Appl. Sci.* 2023, 13, 12265. <https://doi.org/10.3390/app132212265>
- [21] Hutchings, I., Tuladhar, T., Mackley, M., Vadillo, D., Hoath, S. & Martin, G. Links between ink rheology, drop-on-demand jet formation, and printability. *Journal Of Imaging Science And Technology.* **53** pp. 1-8 (2009)

- [22] Guo, Y., Patanwala, H., Bognet, B. & Ma, A. Inkjet and inkjet-based 3D printing: connecting fluid properties and printing performance. *Rapid Prototyping Journal*. **23**, 562-576 (2017)
- [23] Krishnan, J., Deshpande, A. & Kumar, P. Rheology of complex fluids. (Springer, 2010)
- [24] Ulery, B., Nair, L. & Laurencin, C. Biomedical applications of biodegradable polymers. *Journal Of Polymer Science Part B: Polymer Physics*. **49**, 832-864 (2011)
- [25] Barbati, A., Desroches, J., Robisson, A. & McKinley, G. Complex fluids and hydraulic fracturing. *Annual Review Of Chemical And Biomolecular Engineering*. **7** pp. 415-453 (2016)
- [26] Ewoldt, R. & Saengow, C. Designing complex fluids. *Annual Review Of Fluid Mechanics*. **54** pp. 413-441 (2022)
- [27] Öttinger, H.C. *Stochastic processes in polymeric fluids: tools and examples for developing simulation algorithms*; Springer Science & Business Media, 2012.
- [28] J.G Hernández Cifre, Th.M.A.O.M Barenbrug, J.D Schieber, B.H.A.A van den Brule, Brownian dynamics simulation of reversible polymer networks under shear using a non-interacting dumbbell model, *Journal of Non-Newtonian Fluid Mechanics*, Volume 113, Issues 2–3, 2003, Pages 73-96, ISSN 0377-0257. [https://doi.org/10.1016/S0377-0257\(03\)00063-6](https://doi.org/10.1016/S0377-0257(03)00063-6)
- [29] Herrchen, M.; Öttinger, H.C. A detailed comparison of various FENE dumbbell models. *Journal of non-newtonian fluid mechanics* **1997**, *68*, 17–42.
- [30] M. Somasi, B. Khomani, N.J. Woo, J.S. Hur, E.S.G. Shaqfeh, Brownian dynamics simulations of bead-rod and bead-spring chains: Numerical algorithms and coarse-graining issues, *J. Non-Newton. Fluid Mech.* **108** (2002) 227–255.
- [31] Prieto, J.L.; Bermejo, R.; Laso, M. A semi-Lagrangian micro–macro method for viscoelastic flow calculations. *Journal of non-newtonian fluid mechanics* **2010**, *165*, 120–135.
- [32] Medved, A.; Davis, R.; Vasquez, P.A. Understanding Fluid Dynamics from Langevin and Fokker–Planck Equations. *Fluids* **2020**, *5*, 40. <https://doi.org/10.3390/fluids5010040>

- [33] Einstein, A. Uber die von der molekularkinetischen Theorie der Wärme geforderte Bewegung von in ruhenden Flussigkeiten suspendierten Teilchen. *Annalen der Physik* **1905**, *322*, 49–560.
- [34] Karatzas, I.; Shreve, S.E. *Brownian Motion and Stochastic Calculus*; Springer: New York, NY, USA, 1998.
- [35] Coffey, W.; Kalmykov, Y.P. *The Langevin Equation: With Applications to Stochastic Problems in Physics, Chemistry and Electrical Engineering*; World Scientific: Singapore, 2012; Volume 27.
- [36] Arnold, L. *Stochastic Differential Equations: Theory and Applications*; John Wiley and Sons: New York, NY, USA, 1974.
- [37] Kubo, R. The fluctuation-dissipation theorem. *Rep. Prog. Phys.* **1966**, *29*, 255.
- [38] March, N.H.; Tosi, M.P. *Introduction to Liquid State Physics*; World Scientific: Singapore, 2002.
- [39] Mason, T.G.; Ganesan, K.; Van Zanten, J.H.; Wirtz, D.; Kuo, S.C. Particle tracking microrheology of complex fluids. *Phys. Rev. Lett.* **1997**, *79*, 3282.
- [40] Furst, E.M.; Squires, T.M. *Microrheology*; Oxford University Press: Oxford, UK, 2017.
- [41] Klafter, J.; Blumen, A.; Shlesinger, M.F. Stochastic pathway to anomalous diffusion. *Phys. Rev. A* **1987**, *35*, 3081.
- [42] Tuckerman, M. *Statistical Mechanics: Theory and Molecular Simulation*; Oxford University Press: Oxford, UK, 2010.
- [43] Risken, H. *Fokker-Planck Equation*; Springer: Berlin/Heidelberg, Germany, 1996.
- [44] Renardy, M.; Rogers, R.C. *An Introduction to Partial Differential Equations*; Springer Science & Business Media: Berlin/Heidelberg, Germany, 2006.
- [45] Codling, E.A., and Plank, M.J., and Benhamou, S. Random walk models in biology. *J. R. Soc. Interface* **2008**, *25*, 813–834.

- [46] Sarmiento-Gomez, E., Santamaria-Holek, I. and Castillo, R. Mean-square displacement of particles in slightly interconnected polymer networks. *J. Phys. Chem. B* **2014**, *118*, 1146–1158.

- [47] Evans, M.J.; Rosenthal, J.S. *Probability and Statistics: The Science of Uncertainty*; Macmillan: New York, NY, USA, 2004

APPENDIX A

```
%% Constants
D = 1e-2; % diffusion coefficient
dt = 1e-3; % time step
Np = 5e2; % number of particles
NT = 1e3; % number of time steps

%% Generate particle positions
x = zeros(Np,NT);      y = zeros(Np,NT);      z = zeros(Np,NT);
for k=2:NT
    x(:,k) = x(:,k-1) + sqrt(2*D*dt)*randn(Np,1);
    y(:,k) = y(:,k-1) + sqrt(2*D*dt)*randn(Np,1);
    z(:,k) = z(:,k-1) + sqrt(2*D*dt)*randn(Np,1);
end

%% Calculate MSD
lag = round((1/3)*NT):round((2/3)*NT);
for k=1:length(lag)
    dx = x(:,1+lag(k):end)-x(:,1:end-lag(k));
    dy = y(:,1+lag(k):end)-y(:,1:end-lag(k));
    dz = z(:,1+lag(k):end)-z(:,1:end-lag(k));
    msd1(k,:) = mean(dx'.^2);
    msd2(k,:) = mean(dx'.^2+dy'.^2);
    msd3(k,:) = mean(dx'.^2+dy'.^2+dz'.^2);
end
```

```
%% Plot MSDs
```

```
plot(lag*dt,mean(msd1'),'linewidth',3)
```

```
hold on
```

```
plot(lag*dt,mean(msd2'),'—','linewidth',3)
```

```
plot(lag*dt,mean(msd3'),'-.','linewidth',3)
```

```
%% Recover D
```

```
fmsd1 = fit(lag*dt,mean(msd1'),'a*x','start',1);
```

```
fmsd2 = fit(lag*dt,mean(msd2'),'a*x','start',1);
```

```
fmsd3 = fit(lag*dt,mean(msd3'),'a*x','start',1);
```

```
fmsd1.a/2
```

```
fmsd2.a/4
```

```
fmsd3.a/6
```

APPENDIX B

Recall that in Figure 2.2, the trajectory of three different particles were plotted. Assume we are interested in determining the x-coordinate of the final position of a particle. From the figure, we would have three different answers: $x = 0.0140$, $x = -0.0526$, and $x = 0.0081$. It is clear that the fact that each plot gives a different answer is a result of the randomness of the process. This simple observation implies that the correct question is not *what is the position of the particle?* but rather *what is the most likely position of the particle?* To answer this, we collect the final position of 1000 particles and summarize them using histograms, like the ones shown in Figure B.1.

To construct histograms, we divide the data into groups or ‘bins’ and count how many realizations fall within each bin. The next question is how to extract probabilities out

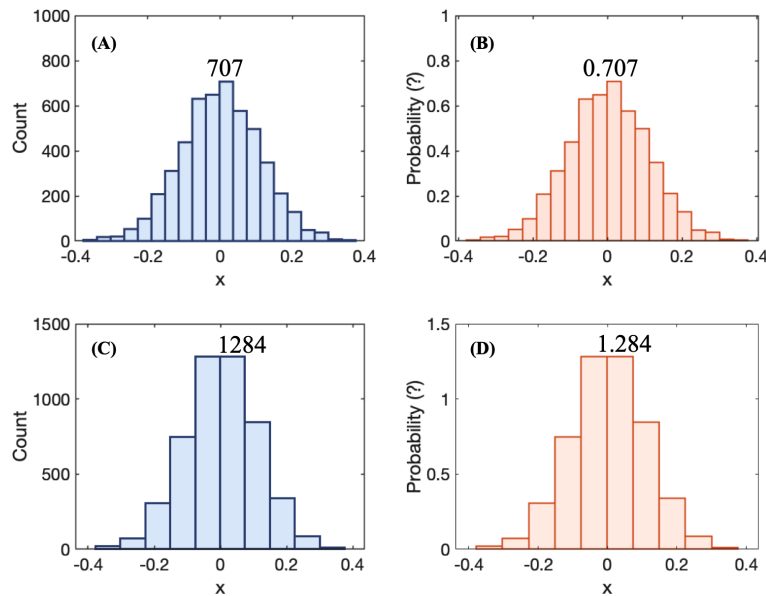


Figure B.1 Histograms of particle positions for 1000 particles. (A) counts using 20 bins; (B) counts from (A) divided by total number of particles; (C) counts using 10 bins; (D) counts from (C) divided by total number of particles.

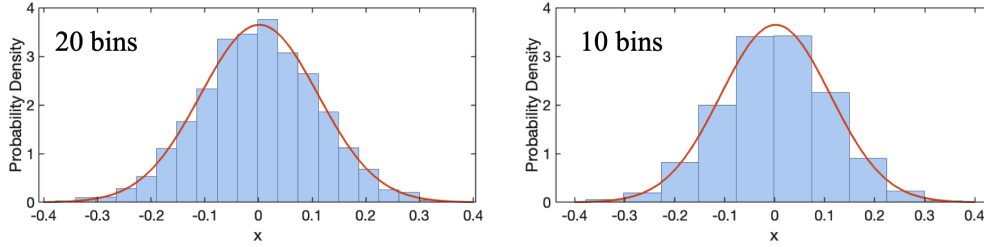


Figure B.2 Normalized histogram of particle positions. The code used to generate these plots can be found in Appendix B.

of these histograms. A first attempt to calculate probabilities is to divide the number of realizations within each bin by the total number of realizations. An inspection of Figure B.1 shows why this is not the correct approach; although both figures **(B)** and **(D)** correspond to the same data, the answer is different depending on the number of bins used.

In order to *transform* the histogram data into probabilities, it is necessary to eliminate the effect of the bin size. This is done by normalizing the histogram using the area of each bin, rather than the counts in each bin. This normalization is shown in Figure B.2. Since the size of the bins does not affect the resulting plot, we could make the size of the bins as small as we wish, to the point of being able to trace a continuous probability density function, represented by the continuous line in Figure B.2, which is unique to the data independently of the number of bins used.

Just as its name indicates, a PDF is not exactly a probability. However, just as one can find the mass of an object by multiplying its density by its volume, we can find a probability by multiplying its probability *density* (PDF) by a range. In this sense, the quantity

$$P(x, t) dx$$

represents the probability that a particle's position is in the range $[x, x + dx]$ at time t .

In addition, working with the continuous form of the PDF, $P(x, t)$, allows us to use integrals to find different probabilities as areas under the curve, as the example given in Figure B.3, or to provide a definition of statistical moments based on PDFs:

$$M_n(x) = \int_{-\infty}^{\infty} x^n P(x, t) dx$$

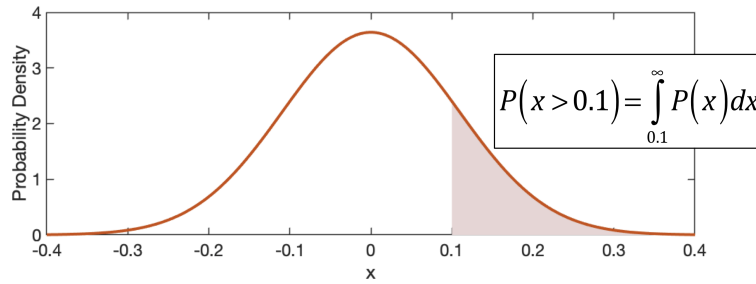


Figure B.3 Calculating probabilities using PDFs.

Note that since the area under the PDF should represent all possible realizations, we have the condition that the area under the whole curve should be equal to one:

$$\int_{-\infty}^{\infty} P(x, t) dx = 1. \quad (\text{B.1})$$

As a final remark, note that not all PDFs are bell-shaped like a Gaussian. The only condition that remains true for all PDFs is that the area under the curve is equal to one as defined in Equation (B.1). In addition, not all PDFs have to define a probability density for every location of the sample space. For a more in-depth review of different probability distribution functions, the reader is referred to [47].

```

%% Computing and Normalizing histogram
[c,n] = hist(x(:,600),20);
c1 = c./trapz(n,c);

%% Fitting to normal distribution
[mu,sigma,muci,sigmaci] = normfit(x(:,600));
Y = normpdf(linspace(-0.4,0.4,1e3),mu,sigma);

%% Plots
bar(n,c1)
hold on
plot(linspace(-0.4,0.4,1e3),Y)

```